A Laboratory Investigation of Nearshorse Turbulence

Mark S. Osler and Ib A. Svendsen

RESEARCH REPORT NO. CACR-04-01
September, 2004

Center for Applied Coastal Research
Ocean Engineering Laboratory
University of Delaware
Newark, DE 19716

ACKNOWLEDGMENTS

I wish to thank my advisor Dr. Ib Svendsen for his guidance and continued support during my time here at the University. In addition, Dr. James Kirby and Dr. Nobu Kobayashi never failed to provide invaluable technical and professional guidance. Michael Davidson was forever prepared to render any help that was needed, be it replacing a potentiometer or conveying a genial word of support and perspective. Dr. Kevin Haas' friendship and assistance with the experimental equipment used in this work is gratefully acknowledged. I would like to thank my family who have been a vital source of support and encouragement during this endeavor. Finally I am grateful for the many friends who I have met while at the lab. Your personalities, insights and laughter transformed an educational experience into and enriching one.

TABLE OF CONTENTS

LIST OF FIGURES

LIST OF TABLES

ABSTRACT

The objectives of the present study are to measure and analyze turbulence generated in a 3-D nearshore wave-current laboratory environment as well as to explore the performance of linear filtering as a means to separate turbulence from the organized wave motion.

Nearshore turbulence is most visibly generated in the surfzone by wave breaking. Surf zone turbulence was analyzed for laboratory data by Svendsen (1987), and through field measurements by George et al. (1994). Attempts have also been made to identify recurring structures in breaking wave turbulence in the form of obliquely descending eddies Nadaoka et al. (1989). However, apart from George et al. (1994), the data for these investigations have all been collected in 2D wave flumes.

The experiments in the present study focus on turbulence in the nearshore flow on a barred beach with waves breaking over the bar and rip currents flowing through the rip channels in the bar. The spatial distribution of the high frequency turbulence is observed.

The extraction of a turbulence signature from a data record which also contains mean flow information and wave orbital velocities is not straightforward. This work explores the application of a linear filtering technique introduced by Shaw & Trowbridge (2001). This linear filter approach employs velocity records from two locations and is based on the assumption that organized wave motion in the two velocity records will be highly coherent while the random turbulent fluctuations will be incoherent.

It is found that for monochromatic waves the linear filter provides a robust tool for extracting the turbulence signal from the data record, although some difficulty was encountered with data taken within the surf zone. The method provided at least an order of magnitude reduction in energy within the primary wave frequencies for approximately 90% of the data sets.

The experiments reveal that high frequency turbulent energy is restricted primarily to the surf zone and just inside the rip channels. Despite the presence of a strong offshore flow, negligible amounts of high frequency energy are present outside the surf zone.

Chapter 1

INTRODUCTION

1.1 Motivation

There is no questioning society's connection to the beaches and coastal oceans that surround us. Whether for military or trade, recreation or commerce, man has endeavored to utilize, enjoy and more recently to understand the nearshore environment. Increasingly, man's development has come into conflict with these dynamic boundaries. As a result, the understanding and prediction of changes in coastal areas has become of paramount importance. Such understanding involves the quantification of many natural forces such as waves, wind, currents and the movement of sandy coastal bottom. Ultimately a prediction of future changes is desired for planning purposes. This prediction then relies on our understanding of these forces.

Like all scientists who attempt to predict what might happen in nature, the coastal engineer is left to rely on mathematical approximations (models) of how the relevant forces will interact, and what the result might be. The more advanced of these models tend to be quite complex in order to account for most of the physics involved. As with any advanced models of fluid flow, the prediction of coastal hydrodynamic forcing must treat turbulence in some fashion. A widely used approach is to apply approximate estimates of the effects of turbulence in the flow, rather than explicitly solving for the details of the turbulent flow. A recent development has been to seek the "complete" solution to the flow at the largest

scales, but to rely again on turbulence approximations for the smaller scales. This approach is termed large eddy simulation (LES). Increased computing power has led the modeler closer to direct numerical simulation (DNS) of the entire flow, whereby the Navier-Stokes and continuity equations are solved directly for the entire domain. However DNS is still limited by computing capabilities, and can handle only very small domains and relatively low Reynolds number flows.

For any computer model, data from the "real world" is required to assess the accuracy of the results. This work seeks to provide some data from inside and outside of the surfzone, with special attention paid to the high frequency turbulent motions. It is hoped that this high frequency information will help provide some guidance for LES modeling of coastal hydrodynamics. More accurate hydrodynamics will eventually permit improvements in predicting sediment transport, and ultimately coastal erosion.

1.2 Outline of Present Work

The aims of the present study are twofold:

1. Evaluate the performance of a linear filter technique for the separation of turbulence from a recorded velocity signal.

2. Using this filter technique, observe the spatial distribution of high frequency turbulence in the presence of a strong offshore flow.

Chapter 2 provides a brief review of turbulent flows and the field and laboratory studies that have sought to measure and analyze turbulence in the coastal environment.

Chapter 3 introduces the concept of linear filters and provides a proof of the approach used in this work.

Chapter 4 describes initial tests of the filter technique applied to flume data.

Chapter 5 describes the main experiment performed in a wave basin. Performance of the filter for this data is examined. The spatial distribution of high frequency turbulence is examined. In addition, a time domain model used to estimate turbulence intensity are compared to the data from the experiment.

The final chapter summarizes the findings of the study and offers conclusions to be drawn from this work.

Chapter 2

TURBULENCE: A REVIEW

2.1 A Description of Turbulent Flow

For low Reynolds number flows, the momentum equations of fluid flow have steady and stable solutions, and such flow is called laminar. Disturbances present in laminar flow are damped by viscous diffusion. With an increase in Reynolds number, the fluid's inertia gained by these disturbances becomes greater than the viscous damping forces, and the flow becomes unstable. If energy continues to be supplied, these instabilities spread and the flow generally become 3 dimensional and unsteady. The presence of strong and unsteady vorticity and pressure gradients throughout the flow, is the hallmark of turbulent flow (Wilcox (1998)).

A brief description of typical turbulent flow characteristics is given below to provide some context for understanding the approach followed in this work. For a detailed discussion of the physics of turbulence, the reader is directed to the classic text by Tennekes & Lumley (1972). An excellent engineering perspective on the analysis and modeling of turbulence is provided by Wilcox (1998).

While a complete definition of turbulence is difficult to formulate, it can be instructive to compile a list of characteristics that turbulent flows exhibit. The three characteristics most relevant to the present work are described below:

1. Irregularity

   Turbulent flows are irregular, or random, and as such are not predictable.

The stochastic nature of turbulence is an important feature, which the filter technique introduced in the next chapter seeks to take advantage of.

2. Range of Scales

   The energy in turbulent flows is present at a wide range of length scales. The largest length scale is usually the dimension of the flow itself, and down through to the very smallest scales where the turbulent energy is damped by viscous forces and transformed into heat. This is in stark contrast to wave motion, where the vast majority of energy is contained in specific length scales. The practical result of the range of length scales in turbulent flow is that it can be difficult to determine, for a given length scale, how much energy should be denoted as turbulence. This is a problem especially when there is more than one process contributing energy at a given scale. The fact that turbulence exists on a range of scales is a primary difficulty for many of the analysis methods covered in Section 2.2.1 below. The approach examined in Chapter 3 was formulated specifically to overcome this problem.

3. Diffusivity

   A dominant characteristic of turbulent flows is the transfer and mixing of momentum, heat and mass. Because of this enhanced mixing capability, the consideration of turbulence is of particular relevance to the problem of sediment suspension and transport. Until the treatment of turbulence is improved in existing predictive models of sediment transport, such modeling efforts will remain qualitative in nature. It is hoped that the present work can be applied to make improvements in the hydrodynamic models which are used to drive predictions of sediment transport.

2.2 Existing Work

2.2.1 Approaches to the Measurement of Turbulence

The extraction of turbulence from a given velocity record can be quite challenging. If one considers a time history of velocity u recorded in the near shore, this record would contain the signature of the mean flow $\bar{u}$, the organized wave motion $\tilde{u}$, as well as the turbulence u', such that $u = \bar{u} + \tilde{u} + u'$.

A classic approach to remove mean properties in periodic flows is phase averaging. Phase averaging is essentially an ensemble average, were the ensemble length is chosen to be equal to the period of the flow, which in this case is the wave period. The phase average is denoted by angle brackets $\langle \cdot \rangle$ and is expressed as

$$\langle u(t) \rangle = \frac{1}{N} \sum_{k=0}^{N-1} u(t + kT) \qquad 0 \leq t \leq T \tag{2.1}$$

where T is the wave period and N is the number of waves used in the calculation. Because the period used in the calculation is fixed, phase averaging requires the measured phenomenon to be highly reproducible. Small changes in the flow, especially phase changes, can result in a damping and distortion of the output (Pedersen et al. (1998)). Phase averaging is essentially useless for non-periodic flows.

A common technique used to study burst phenomena relies on the identification of a "trigger" event in the flow. Based on the trigger, the conditional average (Blackwelder & Kaplan (1976)) is defined as

$$\check{u}(t) = \frac{1}{N} \sum_{k=0}^{N-1} u(t + t_k) \qquad 0 \leq t < min(T) \tag{2.2}$$

where t_k marks the occurrence of the trigger event, $min(T)$ is the smallest time period in the series and N is the number of cycles in the series. This technique has become known as Variable Interval Time Averaging (VITA) and has been used for measurements made in the swash zone (Petti & Longo (2001)).

In addition to the methods above, which operate in the time domain, there are also approaches which function in the frequency domain. An intuitive approach

is a simple high-pass filter at a chosen cutoff frequency (Nadaoka & Kondoh (1982)). As noted in 2.1 above however, turbulent energy is present at a range of frequencies. As a result, any high-pass filtered estimate of turbulence will necessarily neglect turbulent energy that exists at those frequencies which are lower than the chosen cutoff frequency.

Thornton (1979) defined orbital wave motion as that which is coherent with the measured surface elevation. This technique can be difficult to apply to realistic data sets as nonlinearity and directional spreading can reduce the coherence between velocity and surface elevation. In addition, it has been noted that the largest scale eddies do indeed alter the free surface (Nadaoka et al. (1989)). So this approach too would fail to accurately account for energy in the lowest frequencies.

Another frequency domain approach is based on an estimation of energy dissipation (George et al. (1994)) as defined in Taylor's Hypothesis which states

$$E(\kappa) = \alpha \epsilon^{2/3} \kappa^{-5/3} \tag{2.3}$$

where κ is the wave number magnitude, α is a constant and $E(\kappa)$ is the wavenumber spectrum (Tennekes & Lumley (1972)) which can be estimated directly from the measured frequency spectrum. A limiting aspect of this analysis is that it requires Reynolds numbers high enough ($> 10^5$) to realize an inertial subrange, which is indicated by a $-5/3$ slope in the frequency or wavenumber spectrum. It is noted that this criteria is not ensured outside of the surf zone and can also be difficult to meet in the laboratory in general (Longo et al. (2002)).

The final approach to be mentioned is where measured surface elevations are used to predict the associated velocities using linear theory (Rodriguez et al. (1999)). An energy spectrum is computed from the predicted velocities and compared to the spectrum from a set of recorded velocities. This model's dependence on linear theory precludes accurate predictions through the surf zone.

2.2.2 Laboratory Studies

Laboratory investigations of turbulence have traditionally been limited to observations in the swash and surf zones. Svendsen (1987) reviews much of the early work related to surf zone turbulence including Stive & Wind (1982); Nadaoka & Kondoh (1982); Hattori & Aono (1985). This work confirmed that there is only a small variance in the wave averaged turbulent energy over depth in the surf zone, consistent with strong vertical mixing. The result perhaps most utilized from this work is the summary of the relative strength of the three turbulent velocity components (u',v',w') for different types of flows. This summary provides the insight that even for widely varied flows, the relative strength of each component shows only a small variation. Futhermore, this summary has been instrumental in providing a guideline for estimates of the full turbulent kinetic energy, given measurements of only 2 components of the velocity.

Ting & Kirby (1994, 1995, 1996) used flume studies in the surfzone to provide details on the turbulence regime under different breaker types. Other work has documented large-scale turbulent eddies which have a characteristic structure and alter the mean flow field (Nadaoka et al. (1989)). Work with narrow-band irregular waves by Ting (2002) found that turbulence quantities in the inner surf zone are similar despite differences in incident wave spectrum. In the outer surf zone however, differences in the temporal and spatial distribution of wave breaking results in variations in the distribution of turbulence quantities for different wave spectra.

Work in the swash zone (Petti & Longo (2001)) has found that turbulent energy is higher during uprush than during backrush and that the turbulent wave averaged energy flux is essentially directed shoreward.

2.2.3 Field Studies

Experiments in the natural surf zone are quite limited, due primarily to the difficulties inherent in deployment and maintenance of instrumentation in such a

challenging environment. One such study has been conducted (George et al. (1994)), where hotfilm anemometry was used to record velocity. The authors found that Froude-scaled turbulence intensities were slightly smaller than reported in previous lab studies. Better agreement was found when turbulent velocities were scaled by an existing model of bore dissipation in the surf zone. A second field study is that by Rodriguez et al. (1999) which found similarities between the turbulence structure in the surf zone and that in a plane-wake. This work also suggests an expression that relates the length scale of the largest vorticies to the water depth, wave height and wave orbital velocities.

Other field measurements of turbulence are generally from the oceanographic community, and are concerned primarily with estimates of turbulent shear stress and fluxes in the oceanic bottom boundary layer (i.e.Grant & Madsen (1986); Trowbridge et al. (1999); Wolf (1999); Shaw & Trowbridge (2001); Shaw et al. (2001)).

2.3 Summary

The subject of turbulence inside the swash and surf zones has been treated in some detail throughout the past three decades. However there is little data recorded in the absence of broken waves. It remains unclear what level of turbulence should be expected outside of the surfzone. Investigations containing velocity data from outside the surf zone and away from the bottom boundary layer are typically focused on mean flow properties. As a result, the velocities haven't been recorded at a high enough frequency to lend insight into the smaller turbulence scales. It is believed that the 3-D, high frequency velocity data discussed in this work is a first of its kind.

Chapter 3

LINEAR FILTER THEORY

3.1 A New Approach

As noted in Section 2.2.1, there are many approaches to the measurement of turbulence. To be precise the difficulties are not with measurement, but rather with extraction, as the turbulence by definition is contained within the velocity record. Given a velocity record from a point, how can the turbulent component be separated from the original signal? The main difficulty is that turbulence exists over a large range of length and time scales. As a result there are no reliable indicators in either the time or frequency domains which allow the clear distinction of turbulence from the organized motions.

The present work employs a novel approach to this problem which was introduced by Shaw & Trowbridge (2001). Based on the use of linear filters, it was proposed that turbulence can be accurately found by using the velocity records from two different locations. An explanation and derivation of linear filter theory follows in the next section. For now, let it suffice to say that the linear filter provides a means to extract information which is "similar" in the two input time series. This measure of similarity will be the coherence between the two signals, which is discussed in Chapter 4. Shaw & Trowbridge (2001) suggest that the orbital velocities and mean flow will be related at the two locations, while the turbulence will not. The distance between the two locations is important, as they must be far enough apart that the turbulence is indeed "different" (incoherent), while the mean flow

and wave motions are not. A simplified description of the analysis is as follows: the velocity records are passed through the filter, the similar, or coherent, content between the signals is determined, the coherent content is subtracted from the original signal and the remainder is deemed to be the turbulence. Based on this approach, any large scale vorticies, which are coherent across the two locations will not be revealed as turbulence.

This approach is attractive for a number of reasons. It's main benefit is that it works across all frequencies, which is a major improvement over other techniques. Additionally, the linear filter requires no input aside from the two time series of velocity. A final benefit is that the time to process the data is relatively short, taking less than 10 seconds to process an 8 minute series of data on a standard PC. The balance of this chapter provides a derivation of the linear filter used in this work.

3.2 Introduction to Linear Filters

Two functions are said to have a linear relationship if one function can be predicted entirely from the other. A simple example of this would be the equation for a straight line $\mathbf{y} = a\mathbf{x}$. Given the variable $\mathbf{x} = x(1), x(2), \ldots, x(M)$, each value of the variable $\mathbf{y}$ can be found directly. The term "model parameters" is used to denote that information which is required to calculate one variable from another. With this example, the model parameter is simply the slope of the line a. The term filter itself is derived from the fact that the initial data $\mathbf{x}$ is "passed through" (or intertacts with) the model to produce the resulting variable $\mathbf{y}$. While the formula to calculate the slope of a line is well known, we will be concerned with finding model parameters for more complex linear systems.

Consider now a 3-point moving average of the form

$$y(i) = 0.25x(i-1) + 0.5x(i) + 0.25x(i+1) \tag{3.1}$$

where the value of $y(i)$ is determined based on the value of $x(i)$ but also on the values of $x(i \pm 1)$. Notice that the coefficients for each x value are not equal. These coefficients determine how much influence each term will have in the calculation of the average. In this example the value of $x(i)$ is multiplied by 0.5 while the neighboring values are multiplied by 0.25. In essence the central value $x(i)$ has more influence (or is "weighted" more heavily) in the calculation of $y(i)$. Here, the model parameters are the coefficients used in calculating the moving average. The parameters of the filter model will be called "filter weights", which is meant to imply that each coefficient value used in calculating the average may be different from the others.

In preparation for the following section, it is noted that if filter weights are presented in vector form $\mathbf{w} = [w_1, w_2, \ldots, w_N]$, (3.1) can be compacted to

$$y(i) = \sum_{k=1}^{N} w_k x(i + k - 2) \qquad k = 1, 2, \ldots, N \tag{3.2}$$

where $N = 3$.

3.3 The Least Squares Problem

The examples above presume that the input variable ($\mathbf{x}$) and model parameters (w) are known, and it is the second variable ($\mathbf{y}$) which is to be calculated. It stands to reason that it is also possible to determine the model parameters given the two linearly related variables, as we are able to find the slope of a line given two points on it. The remainder of this chapter seeks to demonstrate how the model parameters can be found, based on the *method of least squares.*

Suppose there exists some physical phenomenon characterized by two *known* variables

$$u(i) \equiv \text{system input}$$

$$d(i) \equiv \text{system response}$$

and that the relationship between $u(i)$ and $d(i)$ is linear. For our purposes these variables represent water particle velocities at two locations, where $u(i)$ is the velocity data recorded at position 1 and $d(i)$ is the velocity data recorded at position 2. For clarity we will retain the original variable names used in Haykin (1996). It is then possible to model the response as

$$d(i) = \sum_{k=1}^{N} w_{ok}^{*} u(i-k) \tag{3.3}$$

where

$$w_{ok} \equiv \text{unknown parameters of the model}$$

$$w_{ok}^{*} = \text{the complex conjugate of } w_{ok}$$

In this case, the subscript o denotes the *optimized* or ideal value. This is in contrast to the calculated values that will actually be found. In essence, (3.3) states that the observed response $d(i)$ can be found as a linear combination of the input variable $u(i)$ and the model parameters. Our task is to estimate the actual parameters of the model (w_{ok}) given the two known variables $u(i)$ and $d(i)$.

To determine the model parameters we define the filter weights (which are our calculated estimates of w_{ok}), the estimated output $y(i)$ and the error residual $e(i)$ such that

$$e(i) = d(i) - y(i) \tag{3.4}$$

where

$$y(i) = \sum_{k=1}^{N} w_{k}^{*} u(i-k) \tag{3.5}$$

so that

$$e(i) = d(i) - \sum_{k=1}^{N} w_{k}^{*} u(i-k) \tag{3.6}$$

We would like the calculated filter weights (w_k) to be optimized in a *least squares* sense. In the method of least squares, the filter weights are determined by minimizing the sum of the square of the errors:

$$\varepsilon(w_1, w_2, \ldots, w_N) = \sum_{i=i_1}^{i_2} |e(i)^2| \tag{3.7}$$

where the index limits i_1 and i_2 are chosen in the next section. The problem to be solved is to substitute (3.6) into (3.7) and then minimize the error function $\varepsilon(w_1, w_2, \ldots, w_N)$ with respect to the filter weights w_k. In essence, if $w(k)$ are poorly chosen, then $y(i)$ will be very different than $d(i)$, yielding a large error $e(i)$. With the filter weights well chosen, the estimate $y(i)$ will be close to the actual value and $e(i)$ will be small.

3.4 Solution of the Least Squares Problem

We will take the data from $u(1)$ to $u(M)$ with a total of N filter weights, hence $i_1 = N$ and $i_2 = M$. With this, the error function is given by

$$\varepsilon(w_0, w_1, \ldots, w_N) = \sum_{i=N}^{M} e(i)e^*(i) \tag{3.8}$$

Recalling the definition of the error $e(i)$, we split the filter weights into their real and imaginary parts

$$w_k = a + jb_k \qquad k = 1, 2, \ldots, N \tag{3.9}$$

where j is used to indicate a complex variable and satisfies the equation $j^2 = -1$. Substituting into (3.6) yields

$$e(i) = d(i) - \sum_{k=1}^{N} (a_k - jb_k)u(i-k) \tag{3.10}$$

With complex notation in place, we can proceed with the minimization of the error function. As noted above (Section 3.3), this minimization of the error will be achieved through a least squares approach. To find the minimized values of

$\varepsilon(w_k)$ we define the kth component of the gradient $\nabla\varepsilon$ as the derivative of the error function with respect to the real and imaginary parts of the filter weight w_k

$$\nabla_k\varepsilon = \frac{\partial\varepsilon}{\partial a_k} + j\frac{\partial\varepsilon}{\partial b_k} \tag{3.11}$$

Inserting (3.8) into (3.11) yields

$$\nabla_k\varepsilon = \sum_{i=N}^{M}\left[e(i)\frac{\partial e^*(i)}{\partial a_k} + e^*(i)\frac{\partial e(i)}{\partial a_k} + j\,e(i)\frac{\partial e^*(i)}{\partial b_k} + j\,e^*(i)\frac{\partial e(i)}{\partial b_k}\right] \tag{3.12}$$

For clarity we reiterate that

$$e(i) = d(i) - \sum_{k=1}^{N}(a_k - jb_k)u(i-k)$$

and

$$e^*(i) = d^*(i) - \sum_{k=1}^{N}(a_k + jb_k)u^*(i-k) \tag{3.13}$$

With these definitions in mind we can proceed with evaluating the four partial derivatives in (3.12)

$$\begin{aligned}\frac{\partial e^*(i)}{\partial a_k} &= \frac{\partial d^*(i)}{\partial a_k} - \left[\frac{\partial}{\partial a_k}(a_k + jb_k)\right]u^*(i-k) - (a_k + jb_k)\frac{\partial}{\partial a_k}[u^*(i-k)] \\ &= 0 \qquad - [1]u^*(i-k) \qquad\qquad - (a_k + jb_k)[0] \\ &= -u^*(i-k)\end{aligned} \tag{3.14}$$

$$\begin{aligned}\frac{\partial e^*(i)}{\partial b_k} &= \frac{\partial d^*(i)}{\partial b_k} - \left[\frac{\partial}{\partial b_k}(a_k + jb_k)\right]u^*(i-k) - (a_k + jb_k)\frac{\partial}{\partial b_k}[u^*(i-k)] \\ &= 0 \qquad - [j]u^*(i-k) \qquad\qquad - (a_k + jb_k)[0] \\ &= -ju^*(i-k)\end{aligned} \tag{3.15}$$

$$\begin{aligned}\frac{\partial e(i)}{\partial a_k} &= \frac{\partial d(i)}{\partial a_k} - \left[\frac{\partial}{\partial a_k}(a_k - jb_k)\right]u(i-k) - (a_k - jb_k)\frac{\partial}{\partial a_k}[u(i-k)] \\ &= 0 \qquad - [1]u(i-k) \qquad\qquad - (a_k - jb_k)[0] \\ &= -u(i-k)\end{aligned} \tag{3.16}$$

$$\begin{aligned}\frac{\partial e(i)}{\partial b_k} &= \frac{\partial d(i)}{\partial b_k} - \left[\frac{\partial}{\partial b_k}(a_k - jb_k)\right]u(i-k) - (a_k - jb_k)\frac{\partial}{\partial b_k}[u(i-k)] \\ &= 0 \qquad - [-j]u(i-k) \qquad\qquad - (a_k - jb_k)[0] \\ &= ju(i-k)\end{aligned} \tag{3.17}$$

These four partial derivatives can now be used to evaluate the four main expressions in (3.12)

$$e(i)\frac{\partial e^*(i)}{\partial a_k} = -e(i)u^*(i-k) \tag{3.18}$$

$$e^*(i)\frac{\partial e(i)}{\partial a_k} = -e^*(i)u(i-k) \tag{3.19}$$

$$\begin{aligned}je(i)\frac{\partial e^*(i)}{\partial b_k} &= je(i)(-j)u^*(i-k) \\ &= e(i)u^*(i-k)\end{aligned} \tag{3.20}$$

$$\begin{aligned}je^*(i)\frac{\partial e(i)}{\partial b_k} &= je^*(i)(j)u(i-k) \\ &= -e^*(i)u(i-k)\end{aligned} \tag{3.21}$$

so we can state that

$$\nabla_k \varepsilon = \sum_{i=N}^{M}\Big[-e(i)u^*(i-k) - e^*(i)u(i-k) + e(i)u^*(i-k) - e^*(i)u(i-k)\Big] \tag{3.22}$$

where the first and third terms cancel, and finally

$$\nabla_k \varepsilon = -2\sum_{i=N}^{M} e^*(i)u(i-k) \tag{3.23}$$

For the error function to be minimized with respect to the filter weights, we require that

$$\nabla_k \varepsilon = 0 \qquad k = 1, 2, \ldots, N \tag{3.24}$$

We define the variable $e_{min}(i)$ to be the special value of the error $e(i)$ that results when the filter weights w_k are optimally chosen and hence, the error function $\varepsilon(w_0, w_1, \ldots, w_N)$ is minimized. Based on (3.23) and (3.24), we can state this equivalently as

$$\sum_{i=N}^{M} e^*_{min}(i)u(i-k) = 0 \qquad k = 1, 2, \ldots, N \tag{3.25}$$

We will label the optimized filter weights associated with the least squares condition described in (3.25), as $\hat{w}$ and use this value to restate (3.6) for the case of optimized conditions

$$e_{min}(i) = d(i) - \sum_{t=1}^{N} \hat{w}^*_t u(i-t) \tag{3.26}$$

Where t is now a new dummy variable for summation, introduced in anticipation of the coming substitution. Substituting (3.26) into (3.25)

$$\sum_{i=N}^{M} u(i-k)\left[d^*(i) - \sum_{t=1}^{N} \hat{w}_t u^*(i-t)\right] = 0$$

or

$$\sum_{i=N}^{M} u(i-k)d^*(i) - \sum_{i=N}^{M}\sum_{t=1}^{N} \hat{w}_t u^*(i-t)u(i-k) = 0$$

which yields the set of N simultaneous equations:

$$\sum_{t=1}^{N} \hat{w}_t \sum_{i=N}^{M} u^*(i-t)u(i-k) = \sum_{i=N}^{M} u(i-k)d^*(i) \qquad k = 1, 2, \ldots, N \tag{3.27}$$

The summation over i on the left hand side represents the autocorrelation function of the filter inputs. Specifically we may write

$$\phi(t,k) = \sum_{i=N}^{M} u^*(i-t)u(i-k) \qquad 1 \leq (t,k) \leq N \tag{3.28}$$

and the summation over i on the right hand side represents the cross-correlation between the filter inputs and the desired response. We may write

$$z(-k) = \sum_{i=N}^{M} u(i-k)d^*(i) \qquad 1 \leq k \leq N \tag{3.29}$$

From this, (3.27) can be restated as

$$\sum_{t=1}^{N} \hat{w}_t \phi(t,k) = z(-k) \qquad k = 1, 2, \ldots, N \tag{3.30}$$

In turn, this statement of N simultaneous equations can be cast in matrix notation with the following three definitions

1. The N by N correlation matrix of the filter inputs

$$\mathbf{\Phi} = \begin{bmatrix} \phi(1,1) & \phi(2,1) & \ldots & \phi(N,1) \\ \phi(1,2) & \phi(2,2) & \ldots & \phi(N,2) \\ \vdots & \vdots & \ddots & \vdots \\ \phi(1,N) & \phi(2,N) & \ldots & \phi(N,N) \end{bmatrix} \tag{3.31}$$

2. The N by 1 cross-correlation vector of filter inputs and the desired response

$$\mathbf{z} = [z(-1), z(-2), \ldots, z(-N)]^T \tag{3.32}$$

3. The N by 1 vector of optimized filter weights

$$\hat{\mathbf{w}} = [\hat{w}_1, \hat{w}_2, \ldots, \hat{w}_N]^T \tag{3.33}$$

so that now (3.30) can be compacted to

$$\mathbf{\Phi}\hat{\mathbf{w}} = \mathbf{z} \tag{3.34}$$

Assuming that the inverse matrix $\mathbf{\Phi}^{-1}$ exists, solving for the optimized values of the filter weights is straightforward

$$\hat{\mathbf{w}} = \mathbf{\Phi}^{-1}\mathbf{z} \tag{3.35}$$

(3.35) states that the vector of optimized filter weights $\hat{\mathbf{w}}$ is uniquely defined by the product of the inverse of the correlation matrix $\mathbf{\Phi}$ of the filter inputs and the cross-correlation vector $\mathbf{z}$ between the filter inputs and the desired response (Haykin (1996)). The next section demonstrates how the equations derived above can be applied to the discrete velocity data from our experiments.

3.5 Application of Linear Filter to Data

Again following Haykin (1996) we use the measured input data (velocity at position 1 say) to populate the Nx1 input vector $\mathbf{u}(i)$ as

$$\mathbf{u}(i) = [u(i), u(i-1), \ldots, u(i-N+1)] \tag{3.36}$$

and from (3.28) and (3.36) we recognize that

$$\mathbf{\Phi} = \sum_{i=N}^{M} \mathbf{u}^T(i)\, \mathbf{u}(i) \tag{3.37}$$

Next we define a *data matrix* $\mathbf{A}$ whose transpose is given by

$$\begin{aligned} \mathbf{A^T} &= [\mathbf{u}(N),\ \mathbf{u}(N+1),\ \ldots,\ \mathbf{u}(M)] \\ &= \begin{bmatrix} u(N) & u(N+1) & \ldots & u(M) \\ u(N-1) & u(N) & \ldots & u(M-1) \\ \vdots & \vdots & \ddots & \vdots \\ u(1) & u(2) & \ldots & u(M-N+1) \end{bmatrix} \end{aligned} \tag{3.38}$$

and with this we can state that

$$\mathbf{\Phi} = \mathbf{A}^T\mathbf{A} \tag{3.39}$$

where now the summation in (3.37) is inherent to the matrix multiplication.

We now introduce the *response data vector* $\mathbf{d}$ which contains the system response $d(i)$ (velocities at position 2) for the values of $N \leq i \leq M$ so that

$$\mathbf{d} = [d(N), d(N+1), \ldots, d(M)]^T \tag{3.40}$$

With the definitions in (3.38) and (3.40), we may use (3.29) to express the vector $\mathbf{z}$ (from 3.32) as

$$\mathbf{z} = \mathbf{A}^T\mathbf{d} \tag{3.41}$$

With (3.39) and (3.41) we can find the optimized filter weights $\hat{\mathbf{w}}$ from (3.35). Specifically

$$\hat{\mathbf{w}} = (\mathbf{A}^T\mathbf{A})^{-1}\mathbf{A}^T\mathbf{d} \tag{3.42}$$

With the optimized filter weights determined, the least squares estimate of $\mathbf{d}$ is given by

$$\hat{\mathbf{d}} = \mathbf{A}\hat{\mathbf{w}} \tag{3.43}$$

3.6 Summary

As alluded to in the previous footnote, Shaw & Trowbridge (2001) cast this discussion in terms of velocity data at separate locations, so that the system input $u(i)$ is now the velocity $U_1(i)$ at position (1) and the system response $d(i)$ is the velocity $U_2(i)$ from position (2). Each velocity vector can be decomposed as $U(i) = \tilde{U}(i) + U'(i)$, representing the contributions of the wave and turbulent velocities respectively. It is assumed that the mean flow has been removed prior to data processing.

The central premise is that a linear relationship exists between the *wave induced* velocities at the two positions while there is no relation between the turbulence. Using the notation from above, the data matrix $\mathbf{A}$ is constructed from the velocity at position (1) $U_1(i)$, the response data vector $\mathbf{d}$ is formed from velocity at position (2) $U_2(i)$ and the optimized filter weights are calculated from (3.42). The estimate of the wave induced velocities at position (2) $\hat{U}_2$, follow in turn from (3.43) so that $\hat{U}_2 \approx \tilde{U}_2$ for optimized filter values. From this, an estimate of the turbulent velocity is made by simple subtraction in the time domain, such that $U_1' \approx \hat{U}_1' = U_1 - \hat{U}_1$.

Chapter 4

FLUME EXPERIMENT

As an initial trial of the adaptive filtering technique, tests were conducted in a 2-D flume. These preliminary tests had two purposes: The first purpose was to determine the required separation distance for velocity measurements. It was stated in Section 3.6 that a linear relationship exists between the wave induced velocities at the two positions while the turbulence at these position is not related. Shaw & Trowbridge (2001) uses the coherence between the velocity records as a measure of how well the two signals are related. For the filter to work well we would like the signals to be coherent in the wave frequency bands and incoherent everywhere else. This test was used to find a suitable separation distance where these coherence requirements are met. The second purpose for this experiment was to evaluate the filter's performance under the three different flow conditions which were tested. This initial experiment also served as a trial run for use of the velocimeters and computer controls for the wave paddle and wave gauge.

4.1 Experimental Setup

The experiments were conducted in a two-dimensional, recirculating wave flume in the Ocean Engineering Lab at the University of Delaware. The flume is 30 m long, 0.6 m wide and 1.0 m deep. Water is circulated by a 1500 GPM, 175 psi pump and is passed through a flow straightener, generating a depth uniform current. Flow rate is controlled with a bypass valve that can be used to adjust the percentage of the total flow being circulated.

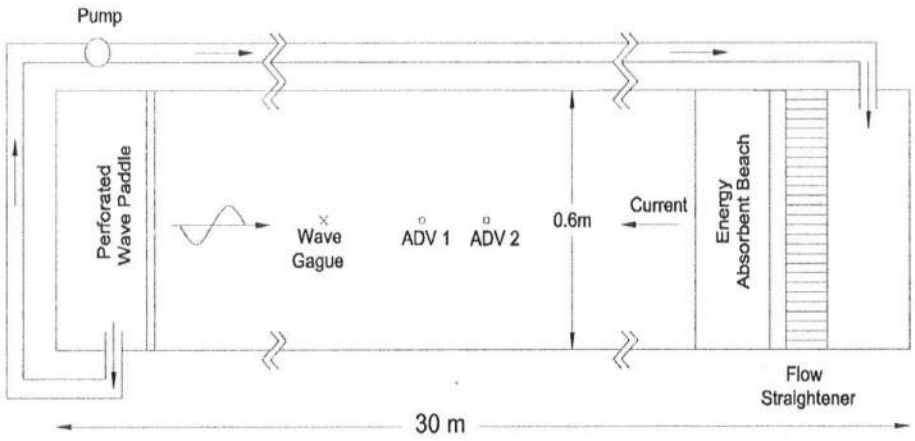

Figure 4.1: Geometry of flume experiment

Waves were generated by a piston type wave maker which was fitted with a perforated paddle to allow the current to pass through. The wave maker accepts a voltage signal from a computer which drives the displacement of the paddle. The paddle can accept any user defined time series of voltage, allowing the production of virtually any wave condition. There is no theory developed relating displacement and generated wave height for the perforated paddle. Although the shape of a desired energy spectrum can generally be realized, the exact values of key wave and spectra statistics can not be calculated a priori. A perforated metal beach at the far end of the flume serves to dissipate wave energy. A still water level of 54 cm was maintained throughout the experiment. The geometry of the experiment is shown in Figure 4.1.

4.1.1 Instrumentation

Velocity was measured using acoustic Doppler velocimeters (ADVs). Instruments built by both Sontek and Nortek were used interchangeably during the experiments. Each ADV was fitted with a 3D, side-looking probe. Data was recorded

at a frequency of 25 Hz. The instrument velocity range was set to ±100 cm/s and a sampling volume of 9 mm was used. Each ADV was placed at the midpoint of the flume and adjusted vertically so that measurements were taken at a depth of 27 cm.

A single capacitance wave gauge was used to record the time history of the water surface elevation. The gauge recorded surface elevation at a frequency of 25 Hz. Energy reflection from the metal beach was not measured.

4.1.2 Procedure

Each ADV's vertical alignment was checked using a level placed along the instrument stem. To ensure that the ADVs were properly aligned with the flow, velocity measurements were made in a monochromatic wave field with no currents. The ADVs were rotated so that the cross-channel velocity was within the error range of the instruments (±1 cm/s for the chosen velocity range). Vertical alignment was rechecked after the instruments were rotated. Each ADV is calibrated at the factory so there was no need to perform a calibration of the ADVs in the lab.

The wave gauge was aligned by eye to face into the waves. The effects of misalignment are removed during the calibration process described below, and should be negligible given that the waves are nearly 2D. The wave gauge calibration was performed automatically by computer. With still water in the flume, the gauge was raised and lowered in 1 cm increments. A voltage reading is taken at each position and a linear calibration curve is produced, relating water level to voltage as reported by the gauge. From this curve, voltage recorded during the experiment can be converted to water surface elevation.

For all tests involving currents, the flow was started once quiet water had been achieved from any previous tests, and was left to run for at least 15 minutes prior to any measurements being taken. This allowed for the dissipation of the surge that is experienced each time the pump is activated. The current strength was 25-30 cm/s for all cases.

All measurements involving waves were taken once the wave train had filled the flume. When waves and currents were being used, the wave maker was engaged after the current flow had stabilized. To avoid the development of standing waves, the wave maker was run for a maximum of 20 minutes at a time.

4.2 Test Conditions

Measurements were made in a total of 3 wave/current conditions. Conditions 1 and 2 recorded velocities in current only and monochromatic waves only respectively. Data from these tests were used to establish the spatial scale at which the signal recorded at each gauge remained coherent. Condition 3 was run with monochromatic waves on an opposing current. Data from these tests were used to evaluate the performance of the filtering technique. Details of each condition are described below.

Condition 1

Velocity measurements were first made in current only. The ADVs were moved apart in 5 cm increments, from a 20 cm separation distance out to 60cm. Tests at distances of 75 and 100 cm were also included. 10 minutes of data was recorded.

Condition 2

Velocity measurements were made in monochromatic waves only. The waves had a period of 2 seconds and hence a kh value of 0.81. The ADVs were moved apart in 50 cm increments, from a 50 cm separation distance out to 200 cm. 10 minutes of data was recorded.

Condition 3

Velocity measurements were made in 2-second monochromatic waves on an opposing current. Measurements were made at 20-, 50- and 100 cm separation distances. 10 minutes of data was recorded.

4.3 Results

Gauge separation distances

Because Condition 1 was simple open channel flow, the velocity record essentially consists of the mean flow and turbulence only. Once the mean velocity is removed, the turbulent velocity is found directly. Because of this, the Condition 1 tests were used to determine how far apart measurements must be made to have a low coherence in the turbulence signal. The coherence for this test is shown in Figures 4.2 and 4.3. The results of the 20-, 50- and 100 cm distances were representative of the range of distances tested and will be focused on here.

The coherence (γ_{12}^2) between two signals is defined by

$$\gamma_{12}^2 = \frac{|\Phi_{12}(n)|^2}{\Phi_{11}(n)\Phi_{22}(n)} \tag{4.1}$$

where $\Phi_{12}(n)$ indicates the spectral estimate defined as

$$\Phi_{12}(n) = F_1^* F_2 \tag{4.2}$$

F_1 is the Fourier transform of the velocity data at position 1 using n points and F_1^* is the complex conjugate of F_1. The coherence represents the percentage of the variance in u_1 that can be ascribed to u_2 through a linear relationship. The values of coherence can range from 0 to 1, where a value near 1 indicates that the two velocities are highly related, while a value near 0 indicates that the velocities are statistically unrelated. The $(1-\alpha)\%$ confidence limits can be calculated from

$$\gamma_{1-\alpha}^2 = 1 - \alpha^{[2/(N-2)]} \tag{4.3}$$

and indicate the level up to which the coherence values can occur by chance (Emery & Thomson (2001)). N is twice the number of realizations used in the spectral estimate. The 95% confidence limits ($\alpha = 0.05$) are shown in each plot.

As Figure 4.2 shows, at 20 cm separation, the signals are coherent out to almost 1.5 Hz. The range of coherence drops to 0.5 Hz at a gauge distance of 50 cm. And when separated by 100 cm, the signals are almost entirely incoherent. As the measurements are taken further apart, the reduction in coherence drops for the higher frequencies. This is logical as the higher frequency components of the turbulence (short time scales) generally have small spatial scales as well (Tennekes & Lumley (1972)). Results from this open channel flow suggest that for instrument separation of 100 cm or greater, the turbulence is incoherent at all but the lowest frequencies.

Condition 2 results (Figures 4.4 and 4.5) indicate that both the horizontal and vertical velocities are highly coherent only at the main wave frequency of 0.5 Hz out to a distance of 2 m.

Consideration of Condition 3 (Figures 4.6 and 4.7) reveals some coherence at frequencies of 1 Hz and smaller, with spikes at the wave frequency of 0.5 Hz as well as the higher harmonics of 1- and 1.5 Hz. As expected, the coherence for Condition 3 looks like a composite of those from Conditions 1 and 2.

Based on these results, it seems that a gauge separation distance of 1 m will satisfy the requirements that the wave induced fluctuations are coherent and the turbulent fluctuations are incoherent.

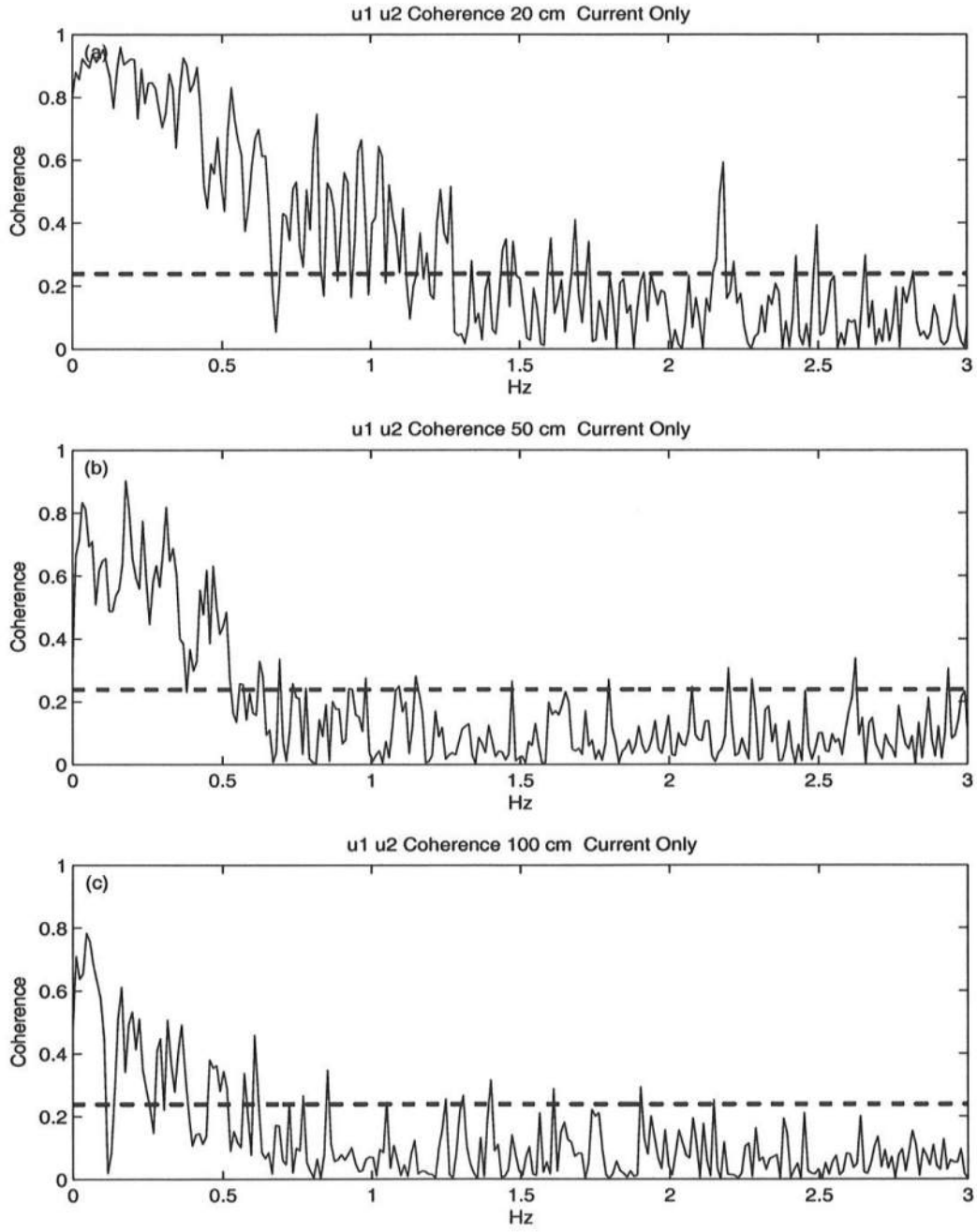

Figure 4.2: Coherence of horizontal velocities at (a) 20 cm separation, (b) 50 cm separation and (c) 100 cm separation. The 95% confidence limit is shown as dashed line. Condition 1 - Currents only

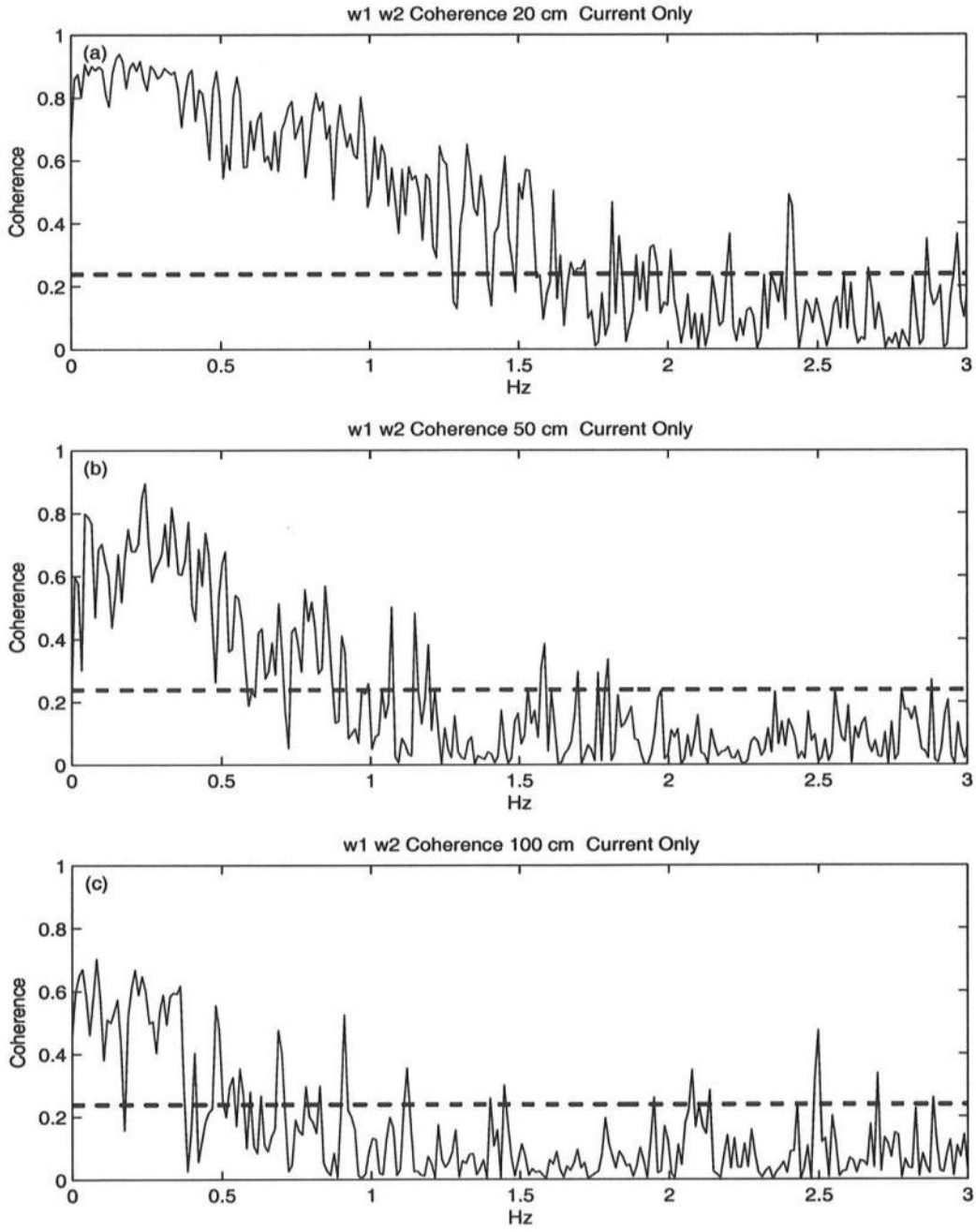

Figure 4.3: Coherence of vertical velocities at (a) 20 cm separation, (b) 50 cm separation and (c) 100 cm separation. The 95% confidence limit is shown as dashed line. Condition 1 - Currents only

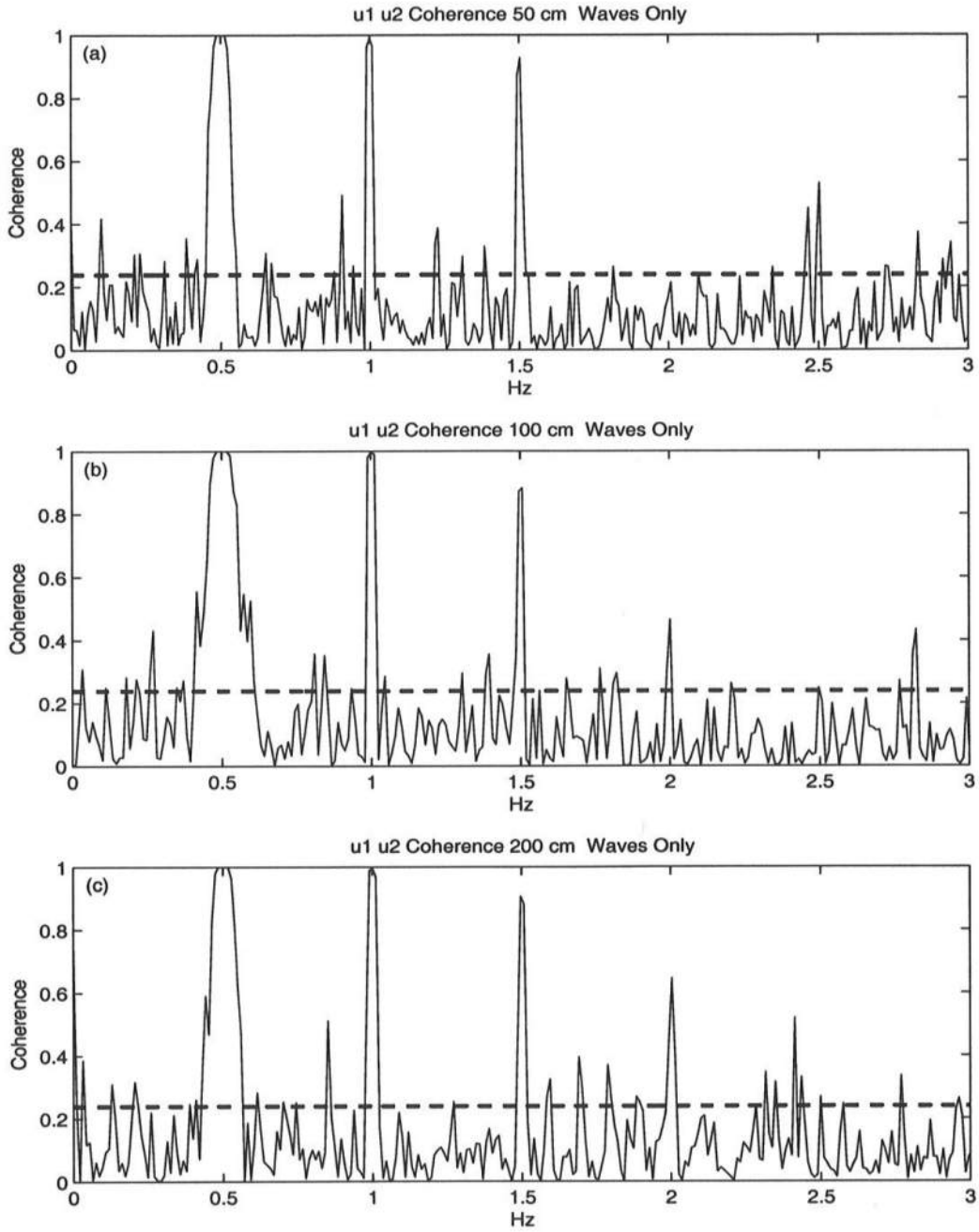

Figure 4.4: Coherence of horizontal velocities at (a) 50 cm separation, (b) 100 cm separation and (c) 200 cm separation. The 95% confidence limit is shown as dashed line. Condition 2 - Waves only

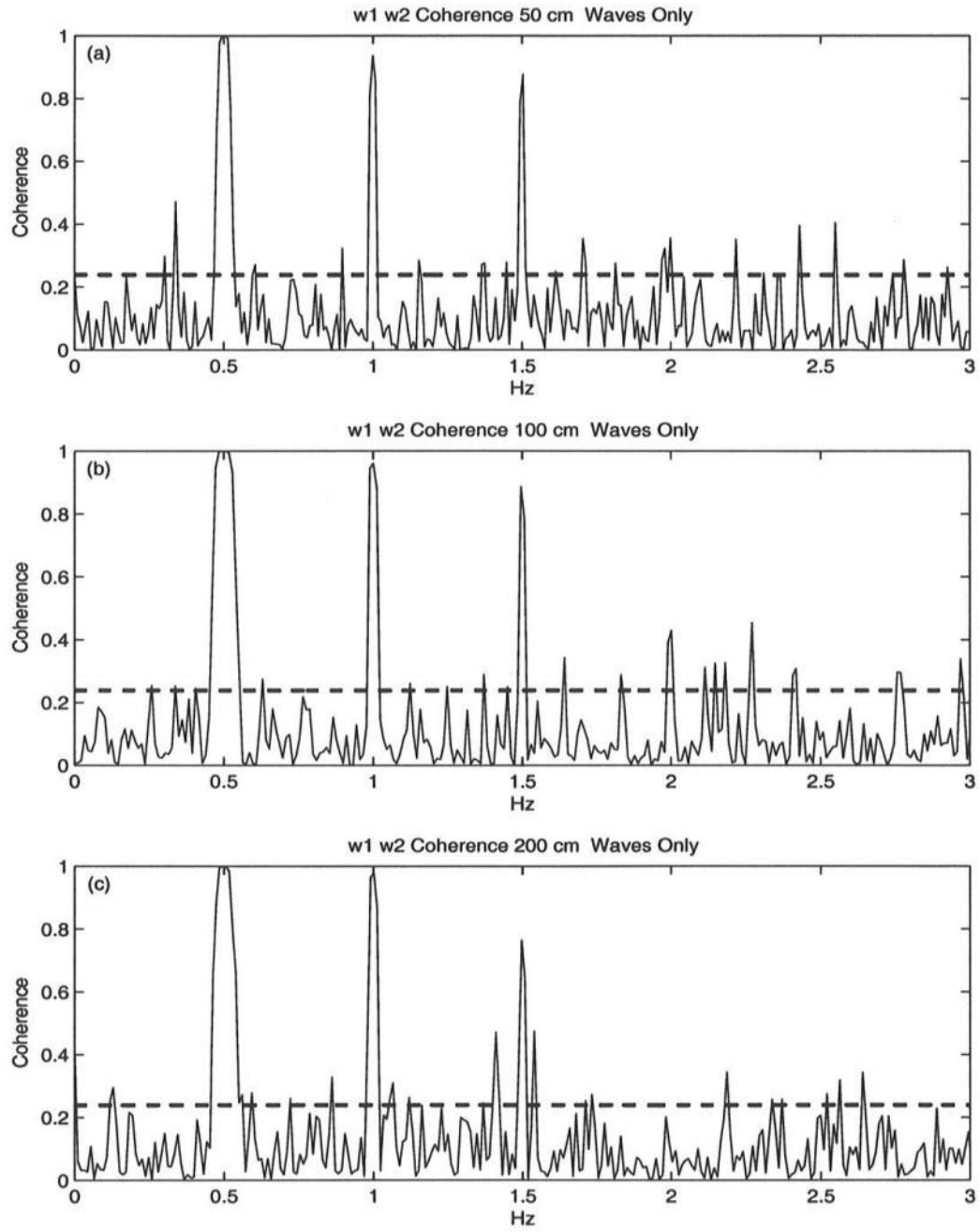

Figure 4.5: Coherence of vertical velocities at (a) 50 cm separation, (b) 100 cm separation and (c) 200 cm separation. The 95% confidence limit is shown as dashed line. Condition 2 - Waves only

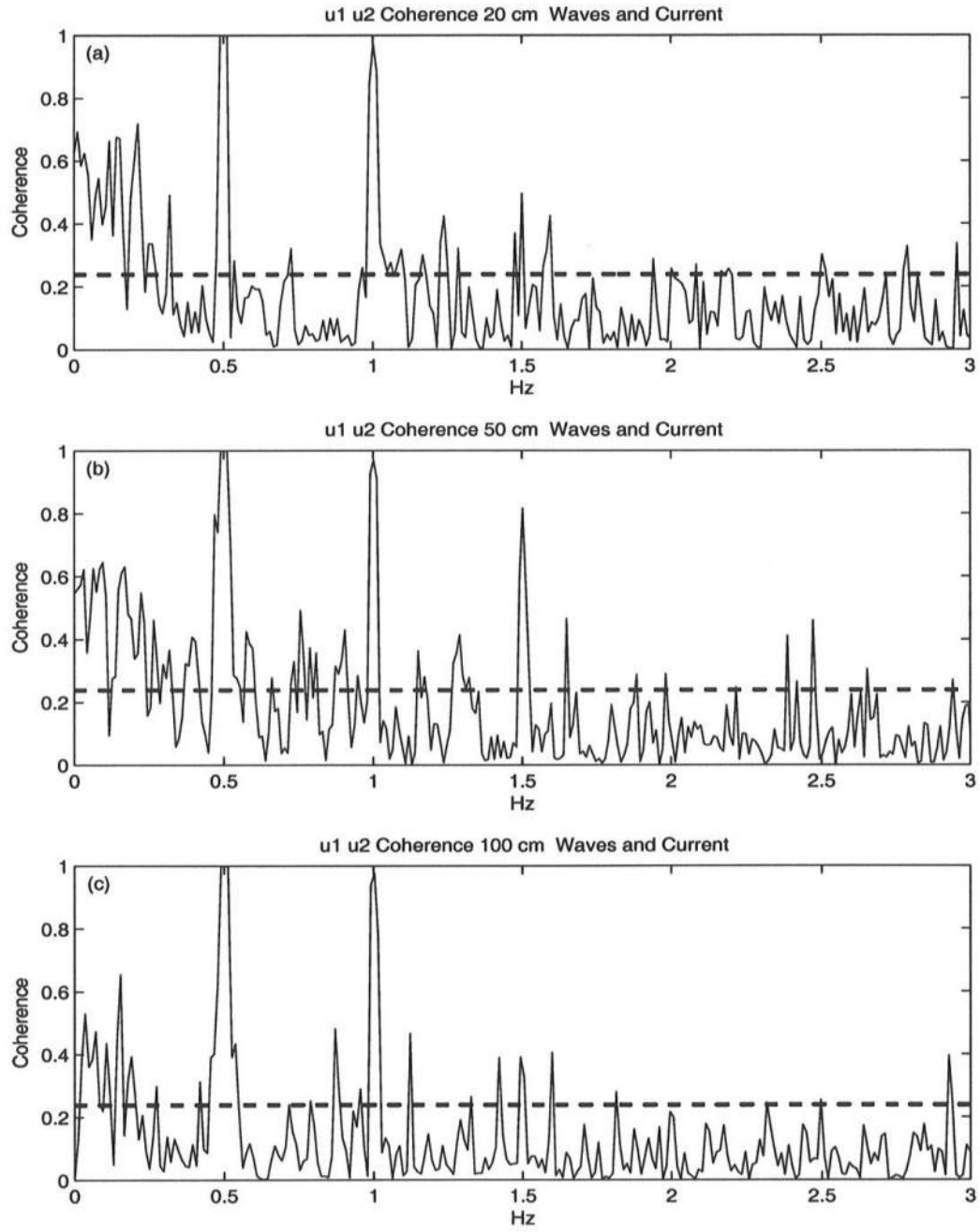

Figure 4.6: Coherence of horizontal velocities at (a) 20 cm separation, (b) 50 cm separation and (c) 100 cm separation. The 95% confidence limit is shown as dashed line. Condition 3 - Waves and Currents

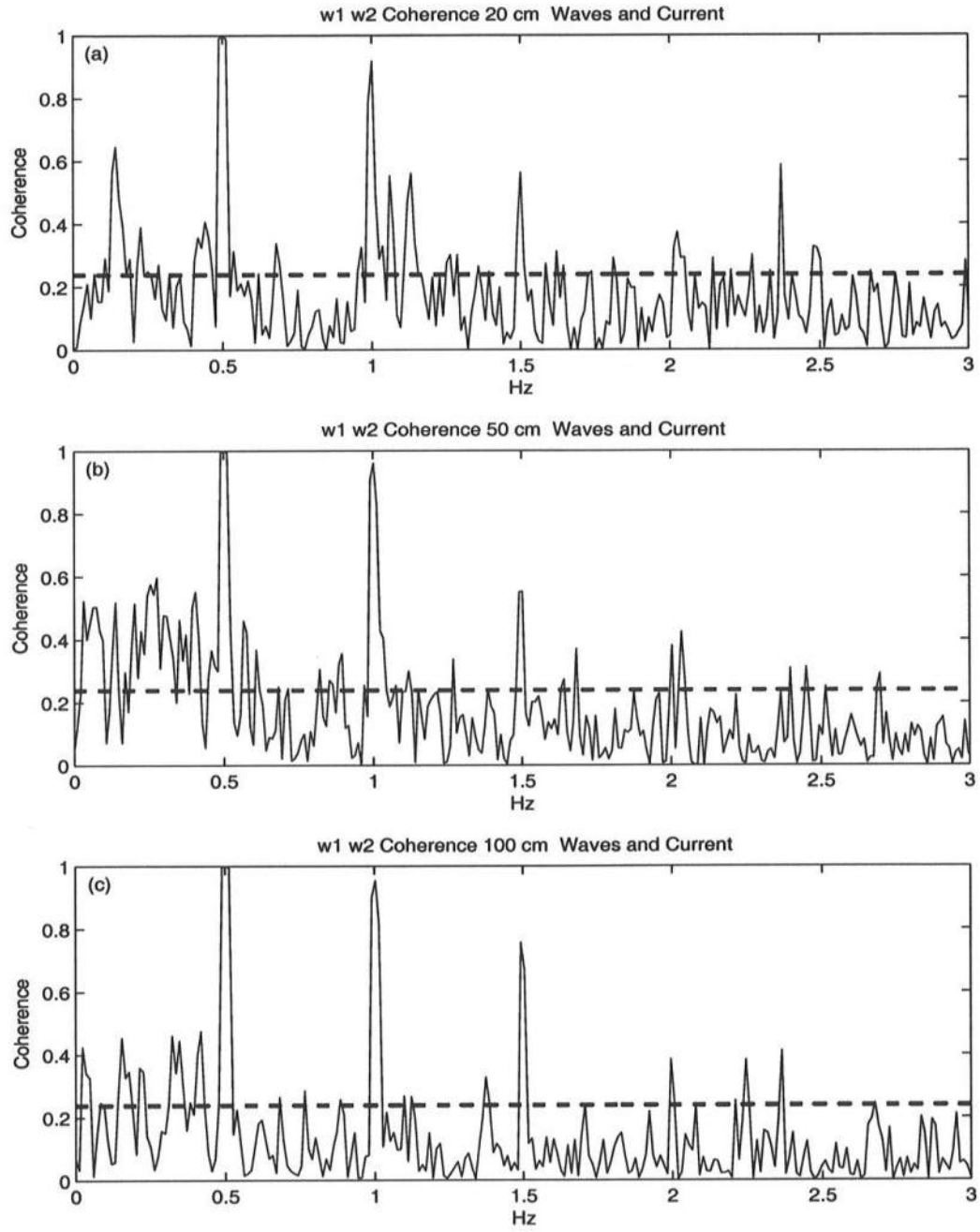

Figure 4.7: Coherence of vertical velocities at (a) 20 cm separation, (b) 50 cm separation and (c) 100 cm separation. The 95% confidence limit is shown as dashed line. Condition 3 - Waves and Currents

Filter performance

As an initial check on the performance of the linear filter, it was applied to a data set from Condition 1 (Figure 4.8) with 100 cm separation. This type of figure is used throughout the work to examine the performance of the linear filter technique. The left side of the plot shows results in the time domain while the right side shows the results in the frequency domain. Transfer into the frequency domain is achieved through a fast Fourier transform (FFT), utilizing Welch's method with 8 overlapping segments (Welch (1967)). The recovered wave signal is what is output from the linear filter. The filter is applied exclusively in the time domain so that the turbulence signal is exactly the original signal less the recovered wave signal. Each realization of the energy spectral density using an FFT is performed after the time domain signals have been constructed. A dashed line is included in the frequency domain plot of the turbulence. A line that carries a $-5/3$ slope on a log-log plot of energy spectral density indicates the presence of an inertial subrange. The inertial subrange is a range of frequencies within which the energy flux across length scales is constant, so that no energy is added to or dissipated from the mean flow (Tennekes & Lumley (1972)). It is further noted that the inertial subrange requires relatively high Reynolds numbers ($> 10^5$). While the presence of this feature in the spectral plots is not of primary importance for this work, the reference line is included for completeness and also as an indicator of the flow intensity. A final note is that the plots in the time domain show a window of only 35 seconds, so that the details of each waveform can be seen clearly; however the filter is applied to the entire 8 minute record.

As expected, essentially all of the energy was ascribed to the turbulence signal. The energy spectrum exhibits the -5/3 slope of the inertial subrange prior to giving way to the noise floor of the instrument.

Data from Condition 3 provided a chance to observe the filter performance

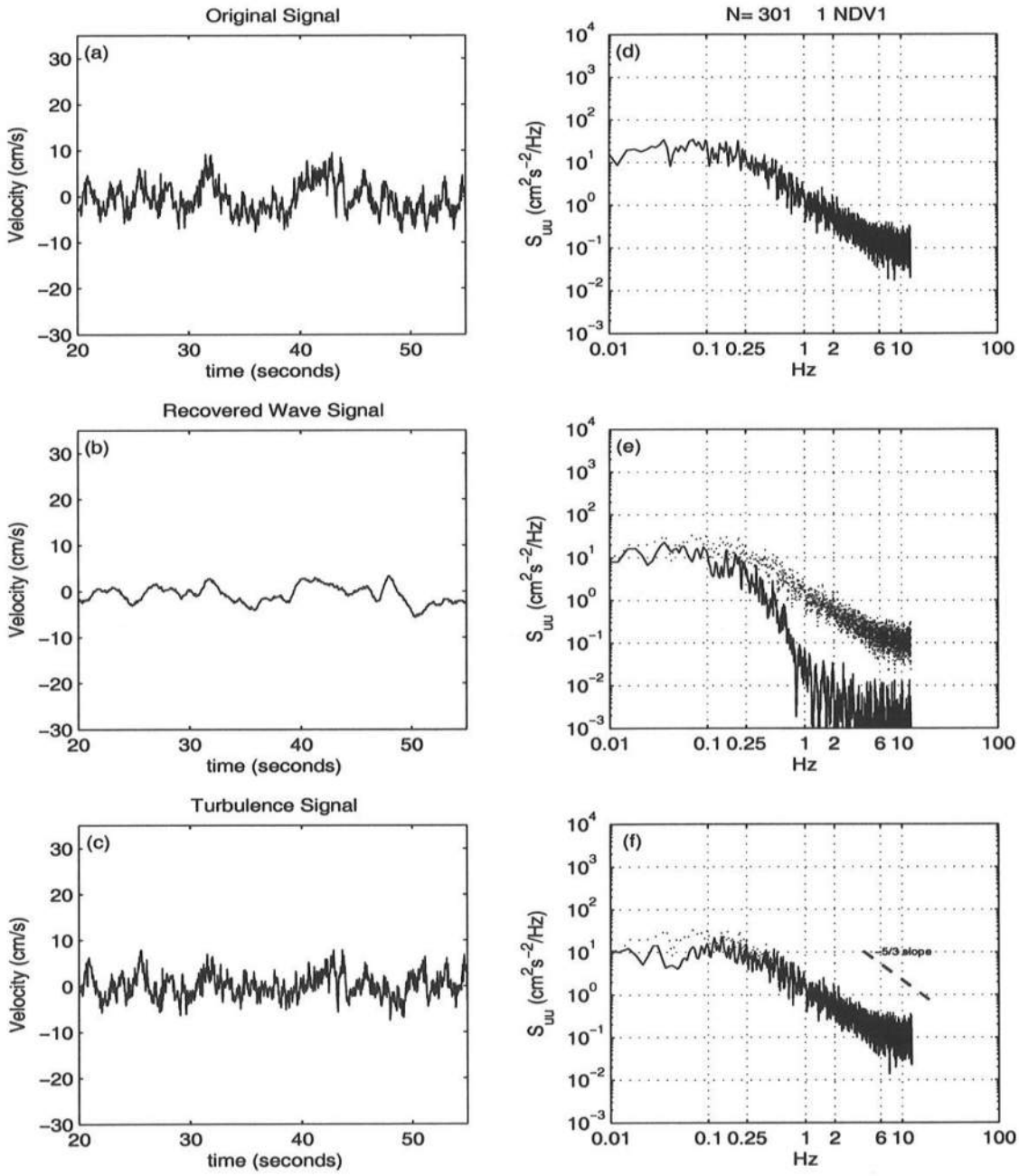

Figure 4.8: Linear filter results. Condition 1 - 100 cm separation (a) Original signal (b) Recovered wave signal (c) Turbulence (d) Energy Spectral Density of Original Signal (e) Energy Spectral Density of Recovered Signal (f) Energy Spectral Density of Turbulence Signal

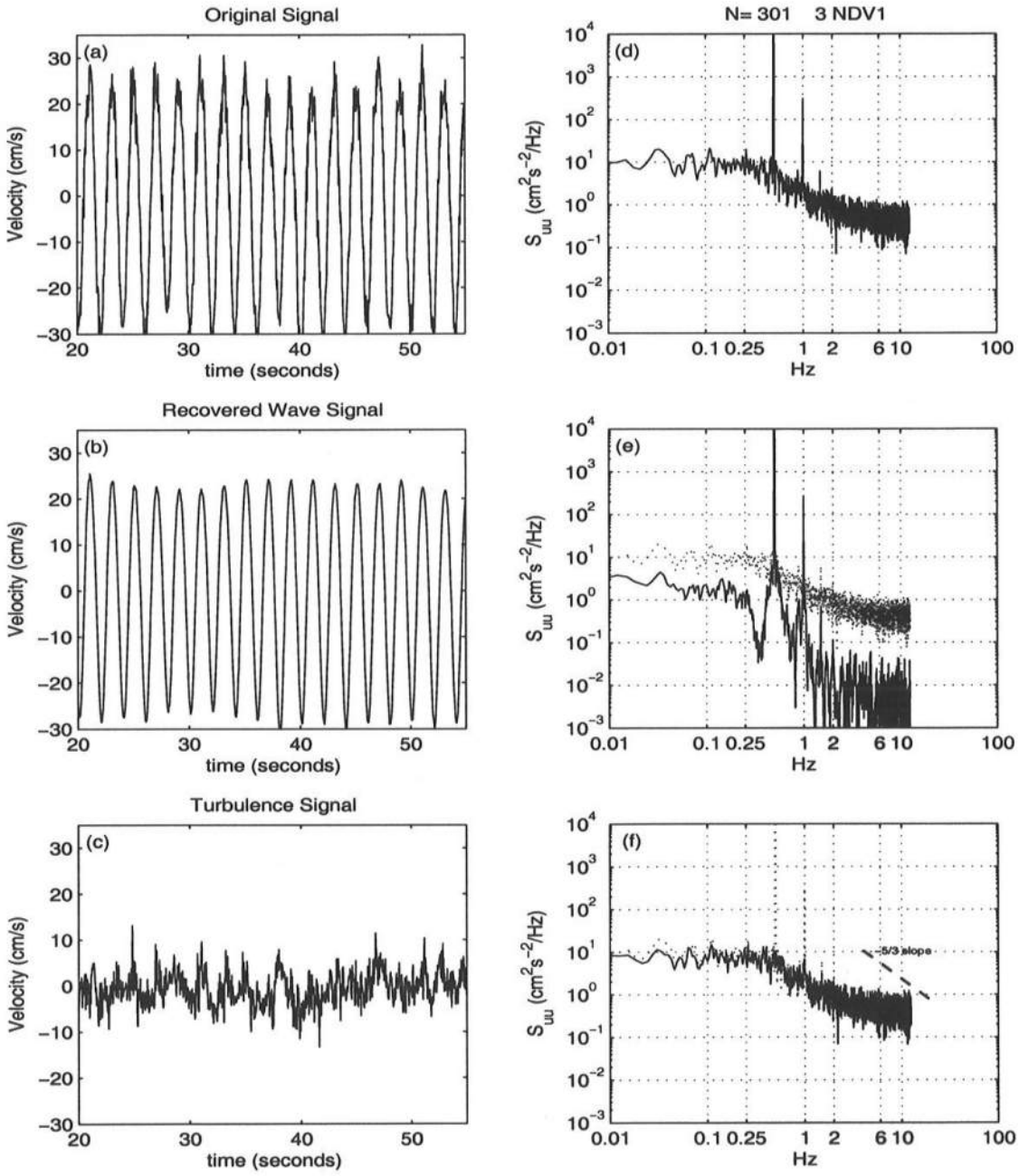

Figure 4.9: Linear filter results. Condition 3 - 100 cm separation (a) Original signal (b) Recovered wave signal (c) Turbulence (d) Energy Spectral Density of Original Signal (e) Energy Spectral Density of Recovered Signal (f) Energy Spectral Density of Turbulence Signal

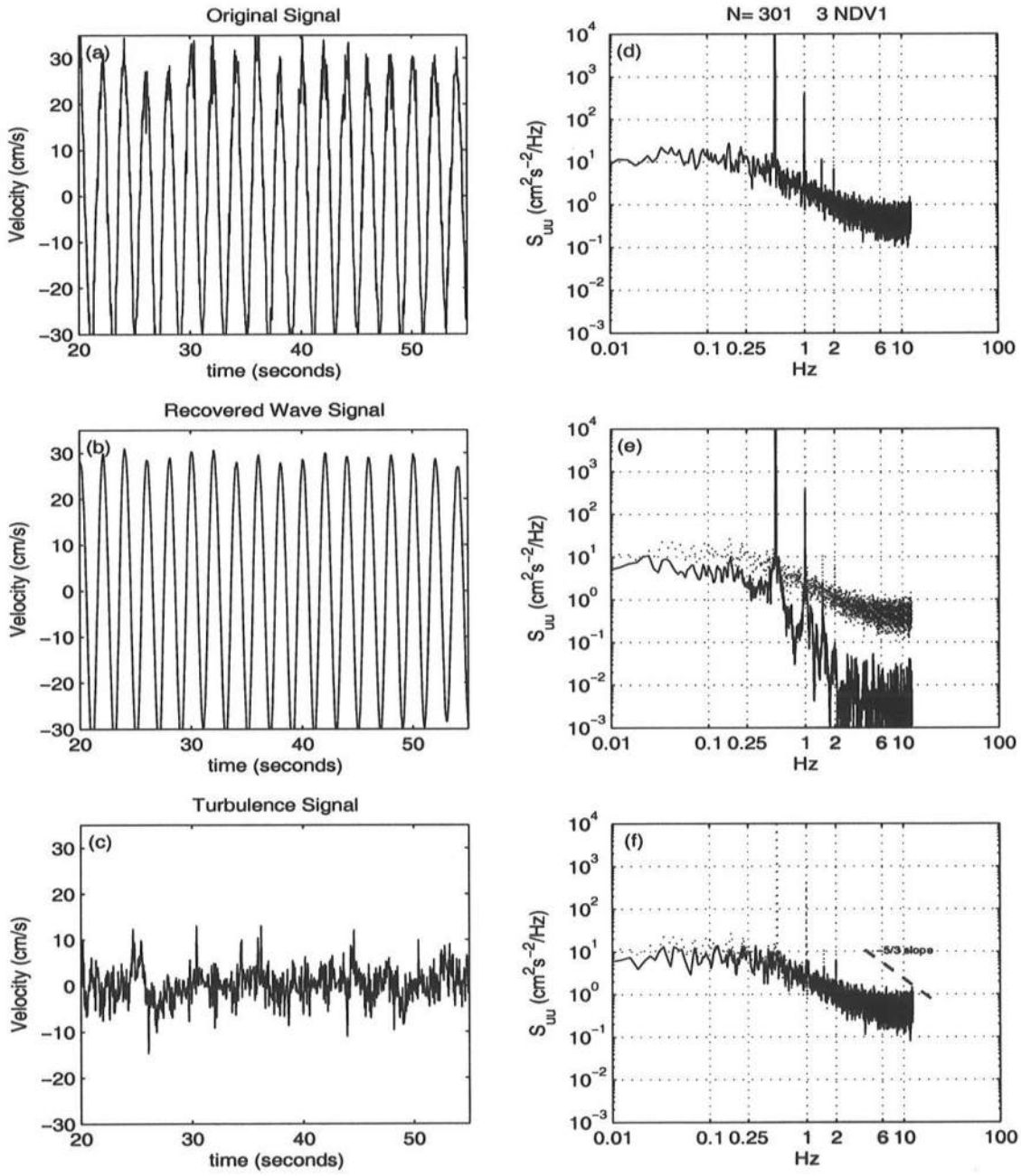

Figure 4.10: Linear filter results. Condition 3 - 50 cm separation (a) Original signal (b) Recovered wave signal (c) Turbulence (d) Energy Spectral Density of Original Signal (e) Energy Spectral Density of Recovered Signal (f) Energy Spectral Density of Turbulence Signal

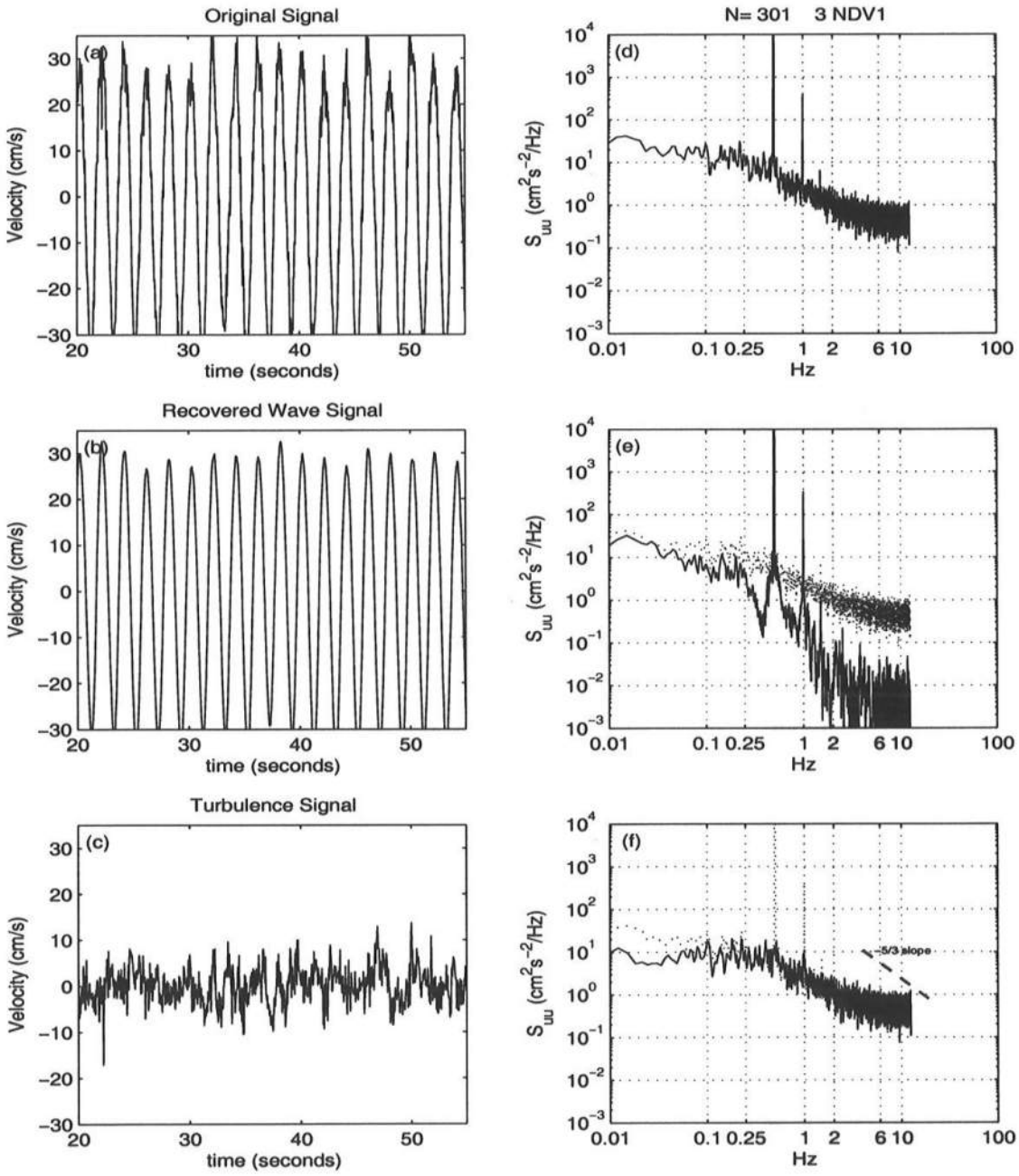

Figure 4.11: Linear filter results. Condition 3 - 20 cm separation (a) Original signal (b) Recovered wave signal (c) Turbulence (d) Energy Spectral Density of Original Signal (e) Energy Spectral Density of Recovered Signal (f) Energy Spectral Density of Turbulence Signal

in monochromatic waves on an opposing current (Figure 4.9). The filter does an excellent job at separating the wave component from the noisy signal. The two energy peaks at 0.5 and 1 Hz are entirely included in the recovered wave signal while the turbulence shows no increase in energy at the wave frequencies.

In order to examine the sensitivity of the filtering technique to the separation distance, data was recorded from Condition 3 at distances of 50- and 20 cm, shown in Figures 4.10 and 4.11 respectively. It can be seen that at a distance of 50 cm, the results look very similar to those from the 1 m separation for frequencies of 0.5 Hz and higher. Below 0.5 Hz however there is a significant increase in energy in the recovered wave signal spectrum. This is expected as the lowest frequencies of the turbulence retain some coherence at a distance of 50 cm. At a distance of 20 cm, the results show another increase in the low frequency energy of the recovered signal, owing to the increased coherence of the low frequency turbulence at this shorter distance. At all separation distances the energy spectrum of the recovered signal is essentially identical above 1 Hz. This is because the turbulence has very low coherence for these high frequencies, even at the closest distance tested.

Filter weights

Once the data has been recorded, the single variable in applying the linear filter is the number of filter weights used N. Figures 4.12 - 4.17 show results for a single case, using various values of N. Results with N values of 1001, 501, 301, 101, 51, 21 are shown. Each of these cases is from Condition 3 with a separation distance of 1 m.

The wave form gets cleaner as the N value dropped from 1001 to 101 and then shows some increased noise continuing down to $N = 21$. Following this same trend the overall spectral density for the recovered signal, excluding the peaks at 0.5- and 1 Hz, falls steadily for the entire range of frequencies as N moves from 1001

to 101. As N moves from 101 to 21, a steady rise in energy occurs at all frequencies, most notably in the frequencies lower than 0.5 Hz.

This comparison indicates that an N value between 301 and 101 is the best choice as it prescribed a majority of the energy outside of the narrow bands of wave frequency to the turbulence. Based on this, a guideline is proposed that the filter length should be chosen such that Ndt is 2-6 times the wave period of interest. A value of $N = 301$ was used for the remainder of the analysis.

4.4 Conclusions

The technique proposed by Shaw & Trowbridge (2001) for the separation of the turbulence signal from organized wave motion was examined in a laboratory flume. The tests indicate that under monochromatic wave conditions, this technique is successful at uncoupling the turbulence signal from the organized wave motion. A gauge separation distance of 1 m was found to be close enough to leave wave induced velocities highly coherent while having the turbulent fluctuations be incoherent. The technique was sensitive to the number of filter weights. As a guideline, it is proposed that the number of filter weights N should be chosen such that Ndt is equal to 2-6 times the wave period of interest.

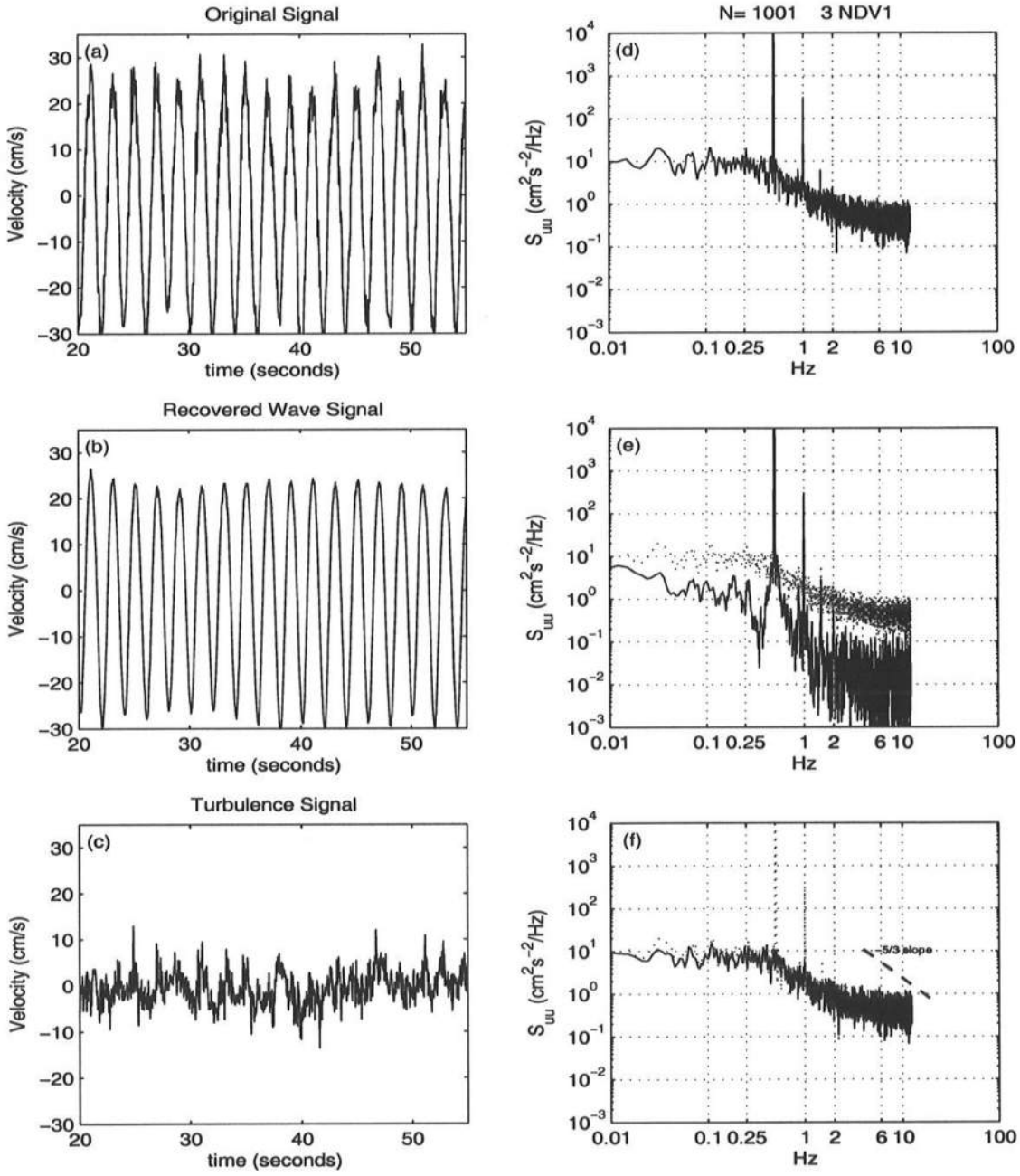

Figure 4.12: Linear filter results. N=1001 Condition 3 - 100 cm separation (a) Original signal (b) Recovered wave signal (c) Turbulence (d) Energy Spectral Density of Original Signal (e) Energy Spectral Density of Recovered Signal (f) Energy Spectral Density of Turbulence Signal

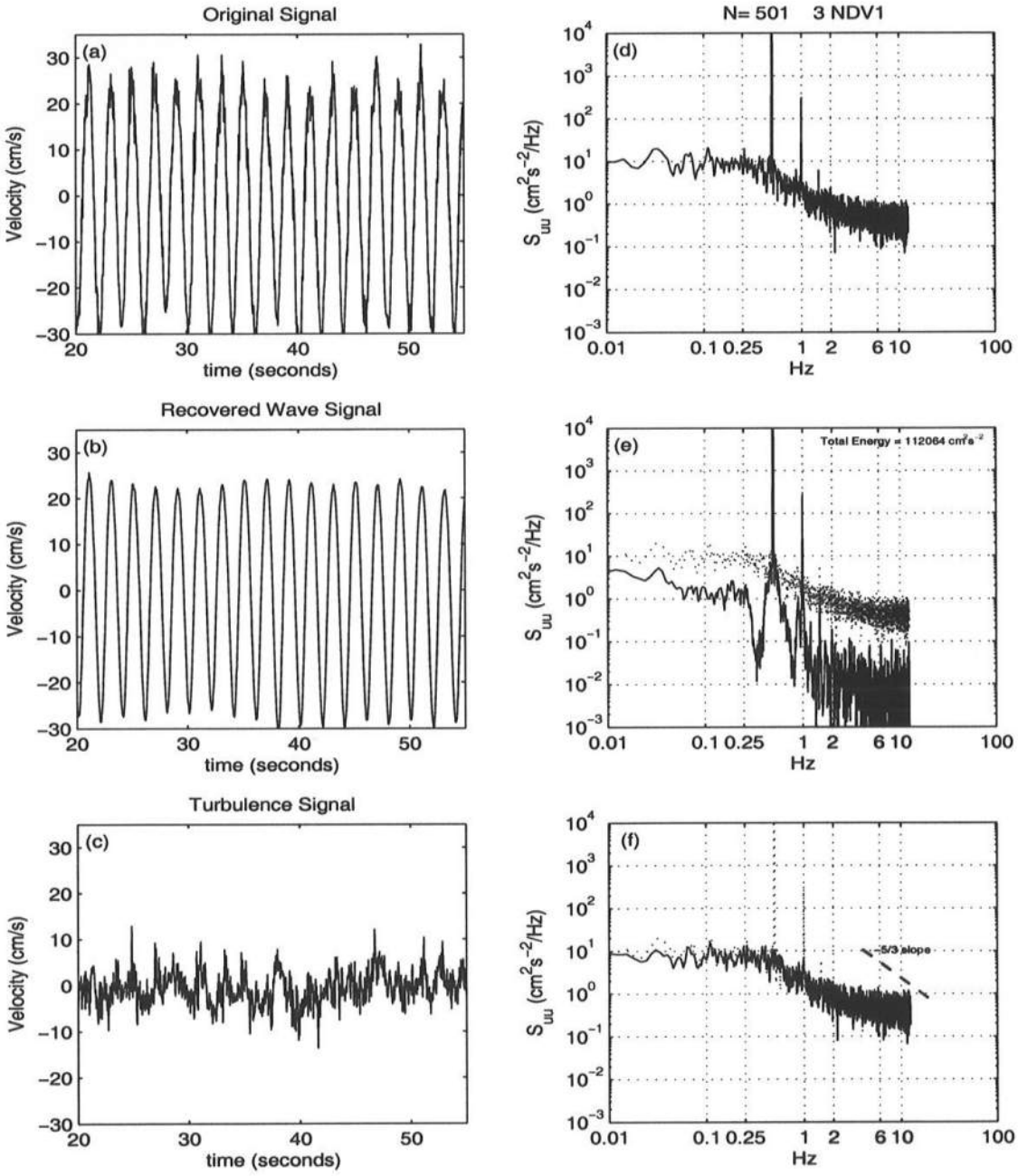

Figure 4.13: Linear filter results. N=501 Condition 3 - 100 cm separation (a) Original signal (b) Recovered wave signal (c) Turbulence (d) Energy Spectral Density of Original Signal (e) Energy Spectral Density of Recovered Signal (f) Energy Spectral Density of Turbulence Signal

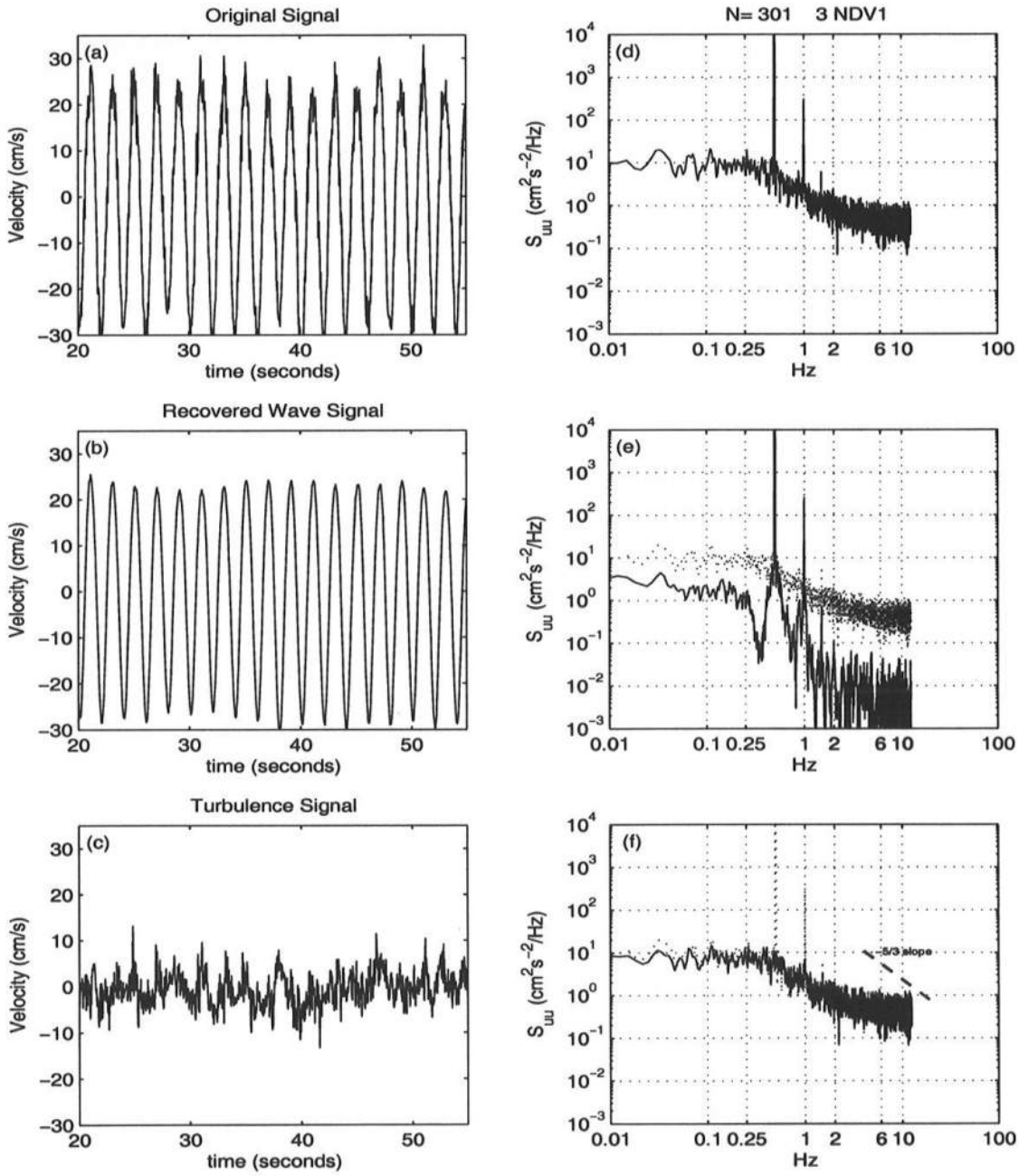

Figure 4.14: Linear filter results. N=301 Condition 3 - 100 cm separation (a) Original signal (b) Recovered wave signal (c) Turbulence (d) Energy Spectral Density of Original Signal (e) Energy Spectral Density of Recovered Signal (f) Energy Spectral Density of Turbulence Signal

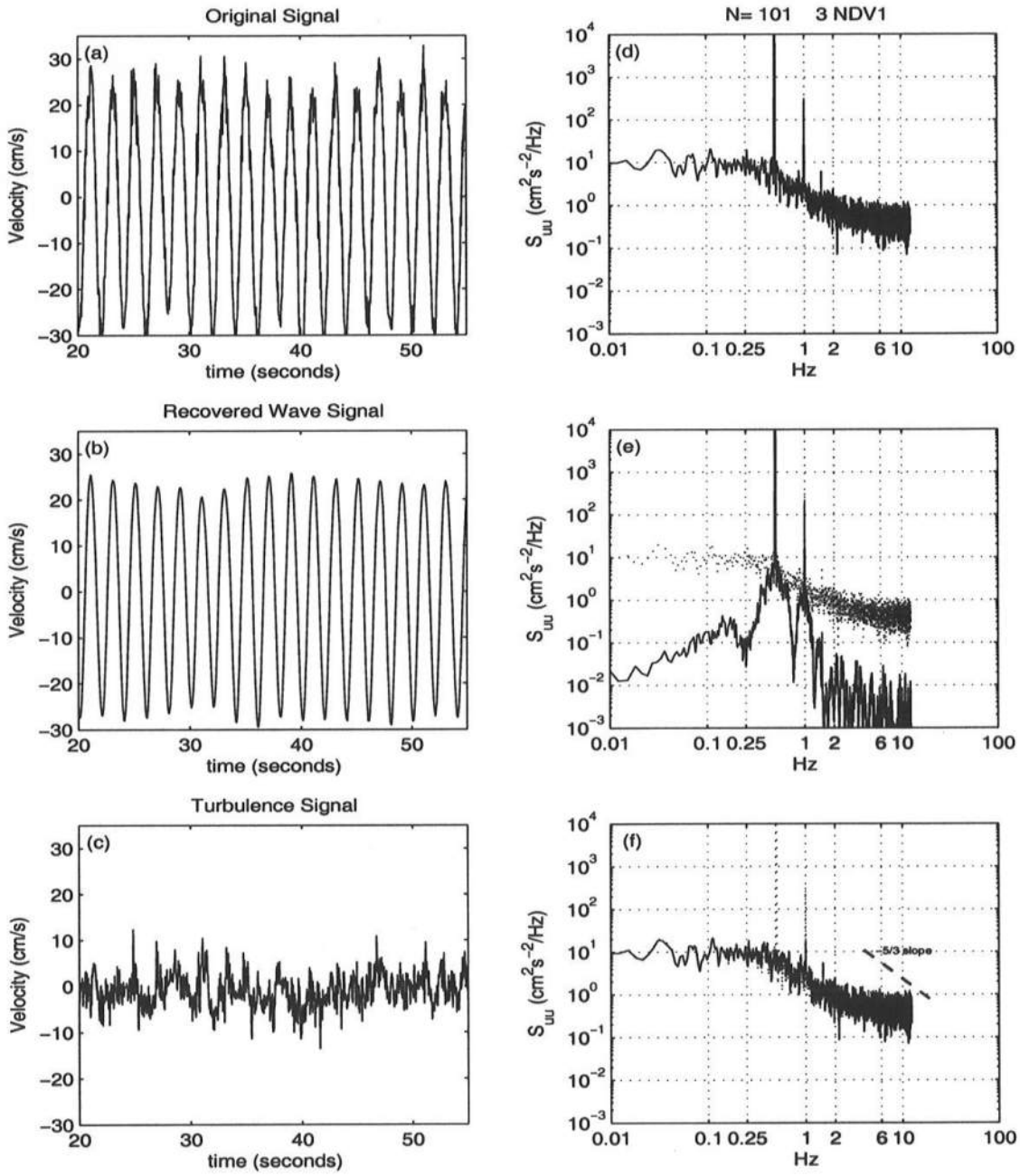

Figure 4.15: Linear filter results. N=101 Condition 3 - 100 cm separation (a) Original signal (b) Recovered wave signal (c) Turbulence (d) Energy Spectral Density of Original Signal (e) Energy Spectral Density of Recovered Signal (f) Energy Spectral Density of Turbulence Signal

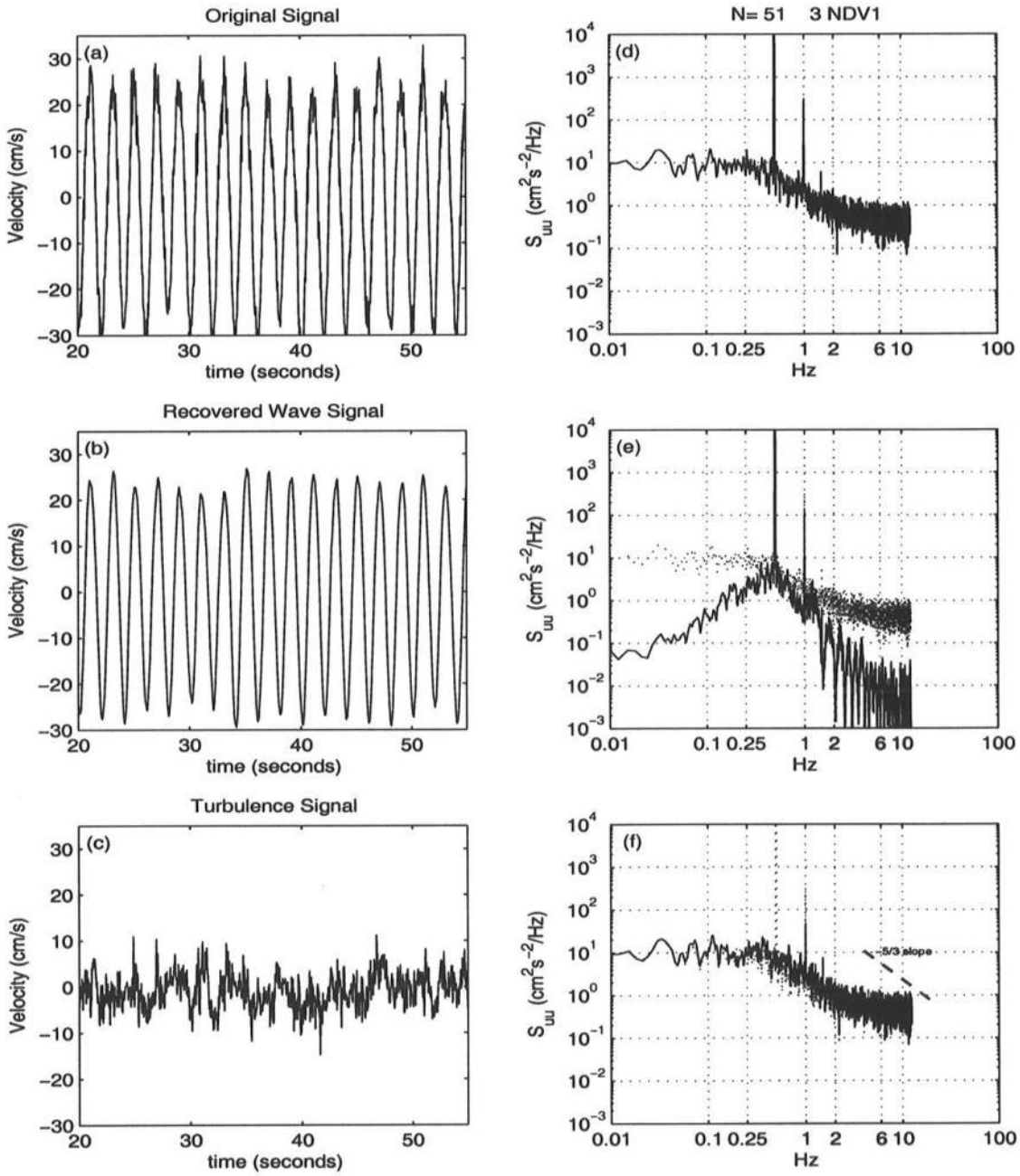

Figure 4.16: Linear filter results. N=51 Condition 3 - 100 cm separation (a) Original signal (b) Recovered wave signal (c) Turbulence (d) Energy Spectral Density of Original Signal (e) Energy Spectral Density of Recovered Signal (f) Energy Spectral Density of Turbulence Signal

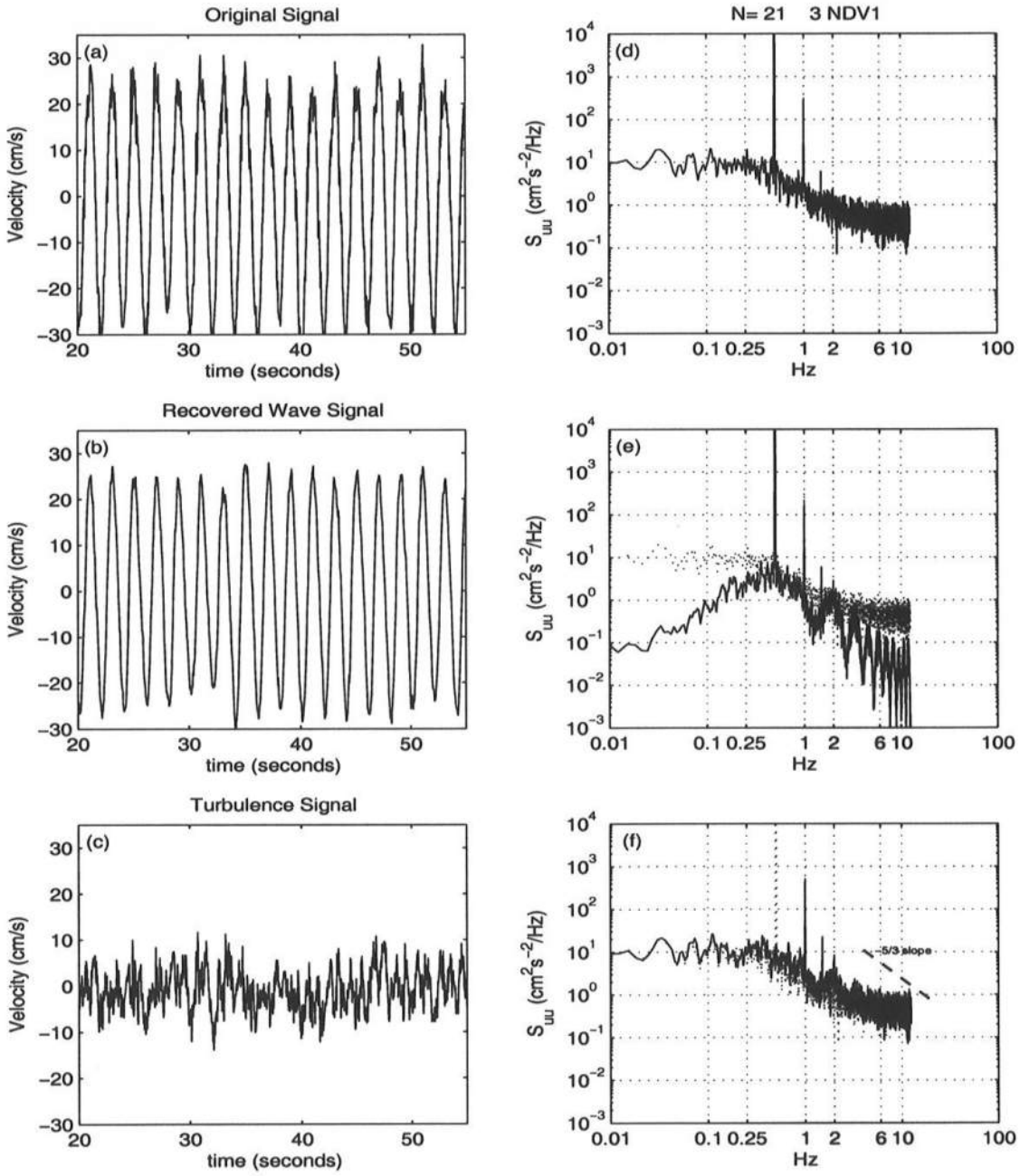

Figure 4.17: Linear filter results. N=21 Condition 3 - 100 cm separation (a) Original signal (b) Recovered wave signal (c) Turbulence (d) Energy Spectral Density of Original Signal (e) Energy Spectral Density of Recovered Signal (f) Energy Spectral Density of Turbulence Signal

Chapter 5

WAVE BASIN EXPERIMENT

The purpose of the wave basin study was to determine the spatial (2-D horizontal) variance of high frequency turbulence inside and outside the surf zone. It was also of interest to examine the performance of the linear filter method introduced in Chapter 4 in a more complex environment, where flows might vary horizontally and wave breaking is present.

5.1 Experimental Setup

This experiment was conducted in the directional wave basin at the Center for Applied Coastal Research at the University of Delaware. The basin measures approximately 18.2 m wide and 17.2 m long. A segmented wave maker of flap type is positioned along the width of the basin at one end. Approximately 2 m in front of the paddles, a steep 1:5 slope transitions into a milder 1:30 slope that runs the remaining length of the basin. Three longshore bars are centered approximately 11.8 m from the offshore wall of the basin. The bars reach a maximum height of 6 cm. The gaps between the bars are approximately 1.8 m wide. A plan view and cross section of the basin are shown in Figure 5.1 with waves incident from left to right.

The basin is equipped with a 34-paddle segmented wave maker. Each paddle has a triangular cross section and is hinged at the bottom. The paddle motions are controlled via a Concurrent 7200 computer control system, where an input file of voltages for each paddle is passed through a digital to analog (D/A) conversion.

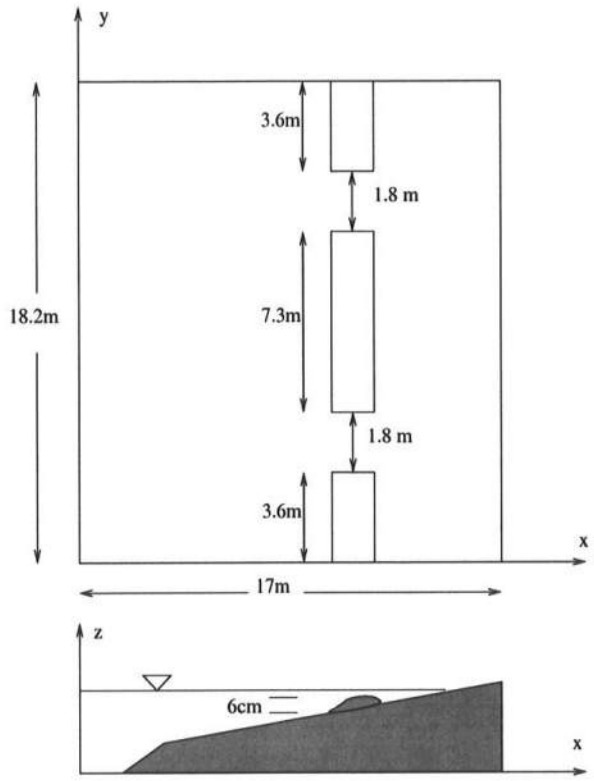

Figure 5.1: Wave basin topography.

The resulting voltages are sent along to the servomotors and each paddle is moved independently. The file of input voltages is created using the Designer Wave Theory by Dalrymple (1989).

5.1.1 Instrumentation

6 capacitance type wave gauges were employed to measure water surface elevation during each of the trials. The calibration of the gauges is performed automatically through the same computer system that controls the wave paddles. With still water in the basin, each gauge is moved up and down in 1 cm increments, with the output voltage being recorded at each elevation. A best linear fit is applied to the resulting outputs and provides a conversion between measured voltage and

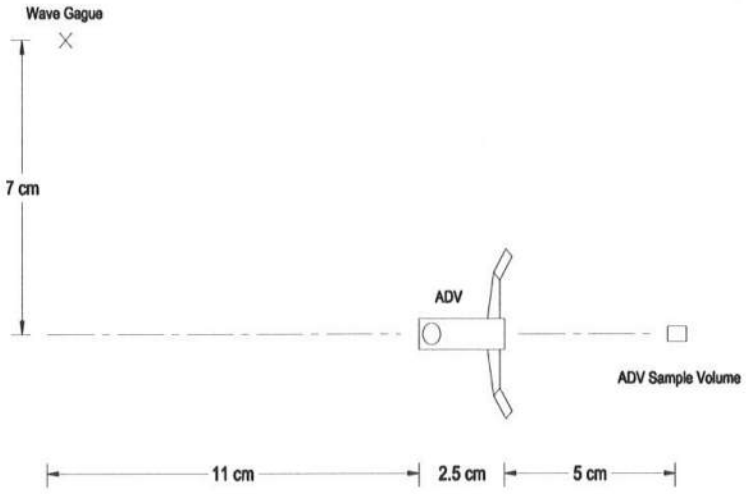

Figure 5.2: Relative locations of typical wave gauge/ADV pair.

surface elevation. Each gauge has a nearly linear response to changes in water surface elevation. Calibration was performed at least twice a day and whenever the gauges were moved. 5 gauges were attached to the instrument bridge and were positioned so as to be paired with the 5 velocimeters as described below. A 6th gauge was placed off shore and served as a reference to provide a measure of repeatability between runs. Short data sets which recorded the still water level immediately prior to running a wave case were run at 10 Hz. All other surface elevation data was recorded at 30 Hz.

Velocities were measured with 5 acoustic Doppler velocimeters (ADVs) manufactured by Nortek. Each probe was fitted with a 3-D, side-looking sensor. The probes were connected to a stand alone PC for data acquisition and no calibration of

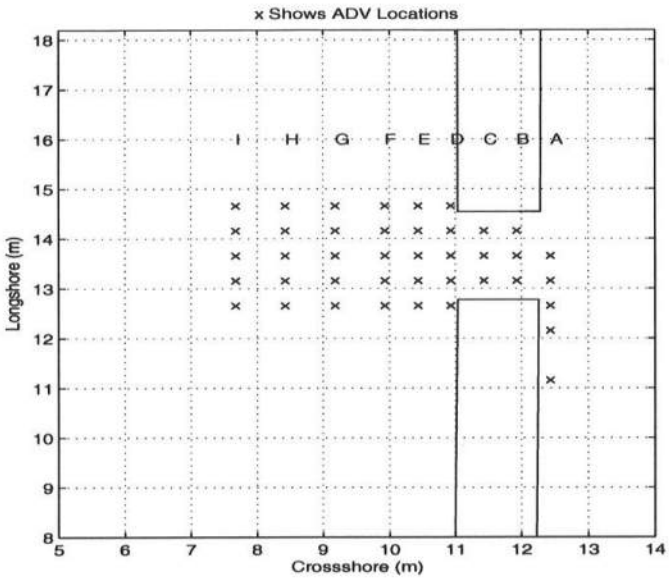

Figure 5.3: Array of ADV measurement locations.

the instruments is required. Each ADV was mounted to the instrument bridge and placed as near as possible to a wave gauge. The geometry of a standard ADV/wave gauge pair is shown in Figure 5.2. For the purposes of analysis, the wave and velocity measurements were considered co-located. The ADVs were placed and aligned by hand. Their positions were measured relative to reference markings which are present on the bottom of the basin. The PC collecting data from the ADVs was also linked to the main Concurrent control system. This connection allowed the start of the ADV data acquisition to be synchronized with the start of the wave gauge data acquisition. All ADV data was recorded at 25 Hz. The five ADV's were mounted in a longshore array with a 0.5 m spacing between each gauge. The single exception to this was made for Position A (see below) where ADV's 1 and 2 were 1 m apart. For each test condition, 9 cross shore locations were measured.

The shoreward location is labeled A with the furthest offshore location labeled I as indicated in Figure 5.3. Positions B and C are inside the rip channel and only

3 ADVs were used here. For each cross shore position, the topmost ADV in Figure 5.3 is numbered as ADV5, with numbers descending to ADV1 for the bottommost ADV. An exception again being for positions B and C, where the numbering runs only from ADV5 to ADV3.

5.1.2 Procedure

A point gauge is mounted on the side of the basin near the wave paddles and this was used to check the water level prior to starting work each day. The water level was adjusted as required. The instrument bridge was moved into place for the desired test plan and waves were run so that the ADV operation could be checked. Once the ADVs were performing properly, the waves were stopped and the basin was left to settle. Once still water had been achieved the following steps were taken for each run:

1. Fine tune instrument positioning if required.
2. Calibrate the wave gauges if they have been moved or this is the first run of the day.
3. Record wave gauge data in still water for 600 steps at 10 Hz (60 seconds) to provide a zero reference level.
4. Record the water temperature for input into the ADV operating software.
5. Initiate the ADV software so that the ADVs will start once receiving the synchronization pulse.
6. Turn on desired wave conditions and let run for 10 minutes so that a steady state condition is reached.

7. Start wave gauge and ADV data acquisition. ADVs recorded 12,000 points at 25 Hz (8 minutes) and the wave gauges recorded 14,400 points at 30 Hz (8 minutes).

8. Once data acquisition has finished, stop the waves and check the data quality.

If the next step is to simply run a different wave condition then restart at Step 3. If the instruments are to be moved, restart at Step 1.

5.2 Test Conditions

Measurements were made for a total of 3 wave conditions. All wave conditions were monochromatic and normally incident. The wave periods and heights for each test are shown in Table 5.1. The wave height listed is the mean wave height recorded at position I. Larger wave heights for Test 3 were desired but could not be realized due to the limited stroke of the wave paddles. The still water level was the same for all tests and provided 4.5 cm water depth over the bar. Each test consisted of an 8 minute data record. This time provided enough data to calculate reliable estimates of the spectral energy density for the high frequency components of the velocity that are the focus of this study.

Table 5.1: Wave Heights and Periods for Tests 1-3

Test	Hm (cm)	Tm (sec)
1	5.52	2.0
2	6.16	1.33
3	7.16	1.33

5.3 Results

5.3.1 Wave Data

Each wave gauge collects a time history of voltage for the duration of an 8 minute recording period. This time history of voltage is converted to a history of water level by means of the constants determined during calibration. Each history of surface elevation then has the mean value (Mean Water Level) removed. Although the raw data is retained for completeness and reference purposes, all subsequent discussion of the wave data refers to statistics determined from the the mean-removed data sets. A zero up-crossing analysis was performed on each data set, to determine the mean wave heights and mean wave periods.

Color contour plots of the mean wave height were constructed by interpolating the mean wave height data from each location throughout a grid which covers the measurement domain. The data fitting employed a triangle-based cubic interpolation. These plots are shown in Figures 5.4- 5.6.

Condition 1 shows a steepening of wave heights just offshore of the rip channel, with some penetration into the channel itself. It is presumed that the steepening is due to wave current interaction as the waves impinge on the strong offshore flow of the rip. This steepening is well balanced across the width of the channel. The maximum mean wave height is 7.7 cm.

Condition 2 shows a similar area of increased wave heights, but it is biased toward the top of the measurement domain. As a result, there are strong gradients of mean wave height in the longshore direction, the steepest of which has a difference in mean wave height of 2 cm between adjacent gauges, a distance of only 0.5 m. The maximum mean wave height is 8.8 cm.

Condition 3 shows a similar bias in position to that in Condition 2, where the increased mean wave heights are centered at the top of the domain. The longshore gradient in mean wave height is even more severe with a difference of 2.6

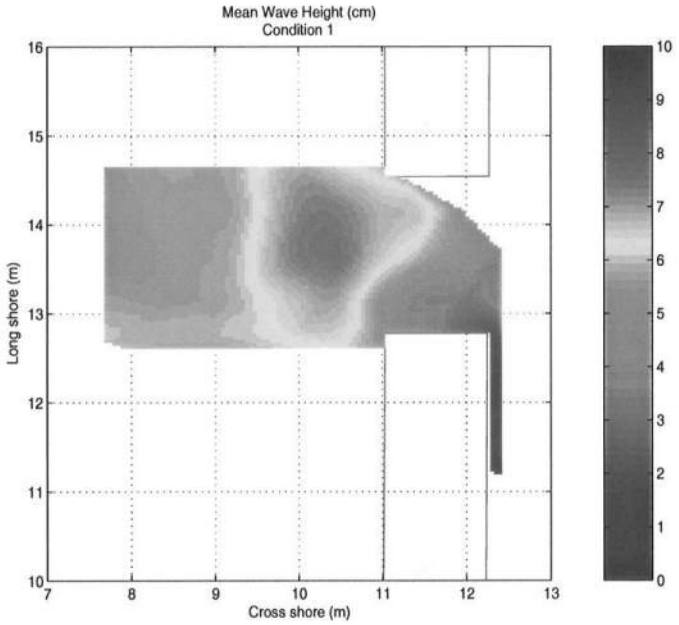

Figure 5.4: Contours of mean wave height. Condition 1

cm recorded between adjacent gauges. The maximum mean wave height is 9.4 cm. It is interesting to note that the steepest gradient in mean wave height for both Conditions 2 and 3 involve the location of the maximum mean wave height.

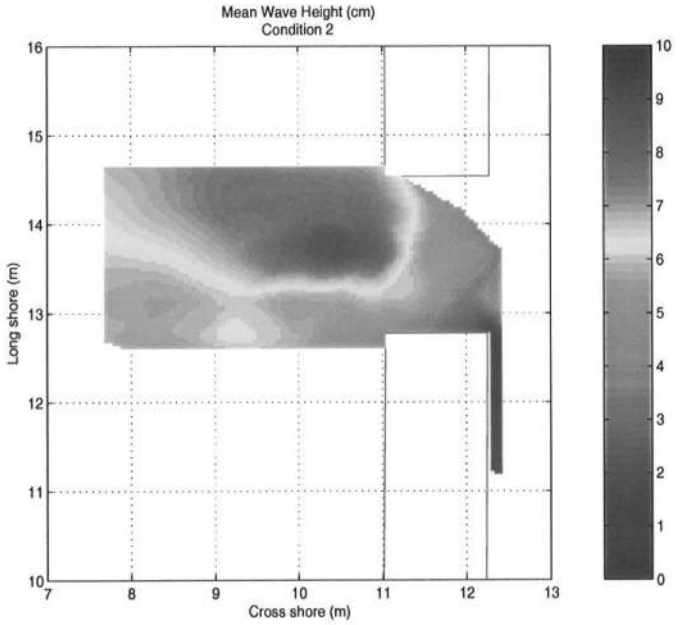

Figure 5.5: Contours of mean wave height. Condition 2

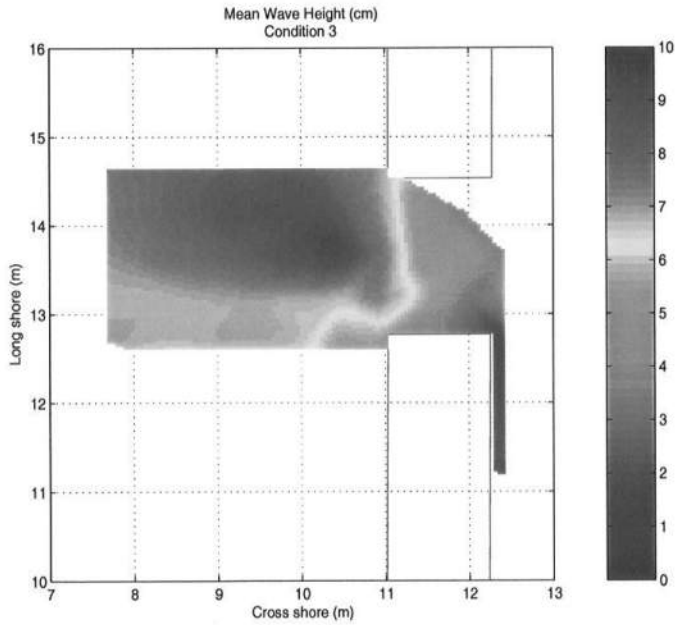

Figure 5.6: Contours of mean wave height. Condition 3

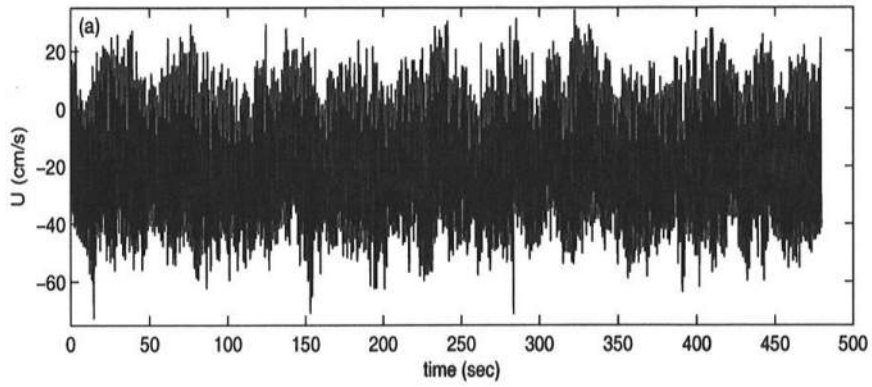

Figure 5.7: Typical velocity record. Position D (see Fig. 5.3) Condition 2

5.3.2 Velocity Data

Each velocity record consists of 8 minutes of data that was recorded at 25 Hz. The quality of the velocity data was determined through consideration of the signal-to-noise ratio (SNR), correlation values and the velocity record itself. Outside of the surf zone, a "clean" velocity signal would have an average SNR above 15 dB, and a correlation value of at least 70. Inside the surfzone, the correlation drops significantly due to the increased turbulence from wave breaking as well as air bubbles being introduced into the measurement area. In these cases, observation of the recorded velocity values was the primary factor in determining data quality. It was generally the case that any problems with data quality were evident from early on in the recording period. If any errors with the data were observed (low SNR, correlation etc.), the velocity records were cleared and restarted for that test.

Mean flow components were calculated to help form a picture of the general pattern of the flows for each condition. A typical velocity record is shown in Figure 5.7. Mean velocities were calculated from each velocity record to provide an understanding of the average flow conditions. Vector plots of these data are shown in Figures 5.8- 5.10.

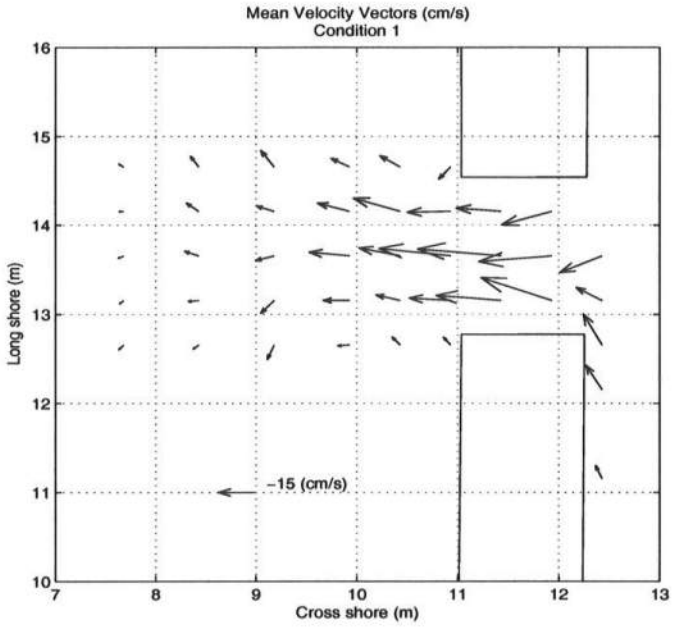

Figure 5.8: Vectors of mean velocity. Condition 1

Condition 1 (Fig. 5.8) shows an organized and almost symmetric flow field. The maximum mean velocity in the channel (Position C, Fig 5.3) is approximately 33 cm/s. The vectors show the flow weakening off shore and turning away from the center of the channel, suggesting the possibility of a gyre on either side of the channel.

Condition 2 (Fig. 5.9) reveals mean flow that is not symmetric about the center line of the channel. There is a clear trend for the flow to turn to the right as it exits the channel. The maximum mean velocity in the channel is 40 cm/s and is again at Position C (Fig 5.3). Even at the edge of the measurement domain, some 3.5 m from the end of the channel, the mean flow is 5-10 cm/s.

Mean flow from Condition 3 (Fig. 5.10) is very similar to Condition 2. Again a bend in mean velocity vectors indicates a strong trend to the right as flow moves seaward of the channel. The maximum mean velocity here is 41 cm/s, essentially

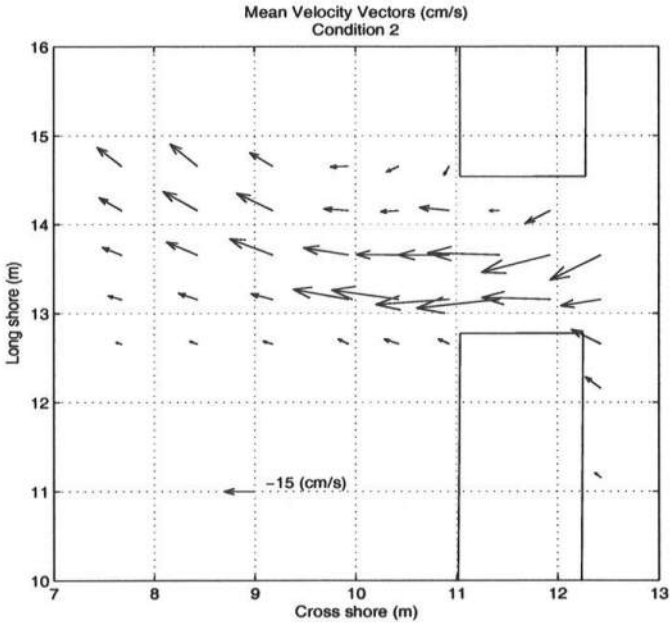

Figure 5.9: Vectors of mean velocity. Condition 2

the same as in Condition 2. This maximum also occurs in the same location.

It is noted that the areas of increased wave heights observed in Figures 5.4-5.6 are colocated with the areas where the rip is flowing strongly seaward. Wiegel (1964) shows that waves encountering an opposing current will maintain a constant period while the wave length, velocity and height will change. For an opposing current such as a rip, the length will decrease while the height increases. This suggests that the increased wave heights are the result of wave-current interaction.

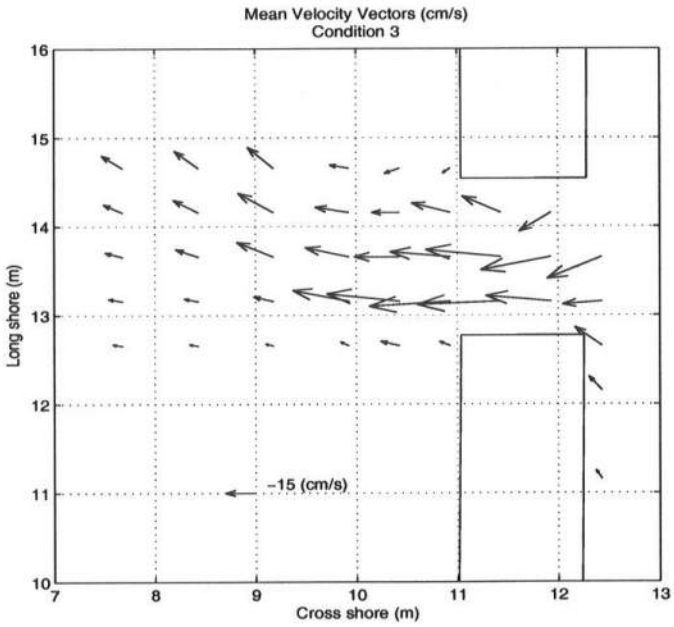

Figure 5.10: Vectors of mean velocity. Condition 3

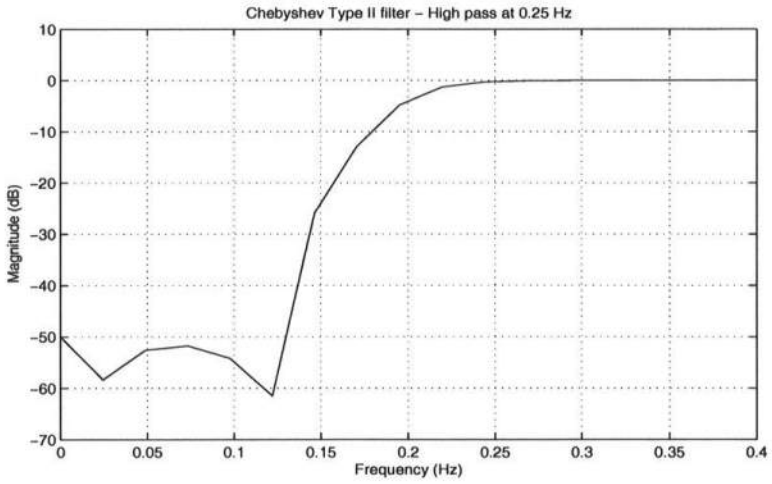

Figure 5.11: Frequency response of the high-pass filter used for the velocity data.

5.3.3 Filter Performance

The performance of the linear filter technique introducted in Chapter 4 was investigated using the data from these tests. The regions covered provide distinct flow conditions to evaluate the effectiveness of the filter. There are areas with relatively weak mean flow and broken waves (Position A), strong flow and broken or breaking waves (Positions B,C,D,E,F) and weak flow and unbroken waves (Positions G,H,I). See Figure 5.3 for the location of each of these positions.

Because the interest in the frequency domain is concerned mainly with the mid-range and high frequency components of the energy spectral density of the velocity, the low frequency components ($f < 0.2$ Hz) were removed from all velocity records. This high-pass filtering was performed using a Chebyshev Type II filter. The frequency response of the filter is shown in Figure 5.11. Although the figure shows response only up to $f = 0.4$ Hz, the filter is monotonic for the entire pass band. This feature is important so that the filtering does not alter the amplitude of the passed frequency components in the original signal.

Once the data was high-pass filtered, it was then passed through the linear

filter as described in Shaw & Trowbridge (2001) and tested in Chapter 4. A typical result is shown in Figure 5.12.

As described in Section 4.3, the left side of the figure shows the time domain results of the linear filter, while the right side displays the energy spectral density of each time series.

This result is chosen as an average performance of the filter. The recovered wave signal is noticeably free of high frequency fluctuations and indeed, the FFT reveals that significant energy is limited to the two prominent peaks, representing the wave period of 1.33 sec ($0.75Hz$) and the first two harmonics. All energy outside the wave frequencies enjoys a reduction of at least 1 order of magnitude. The energy outside the wave frequencies is realized in the turbulence signal. In addition to this energy however, there exist peaks of energy at the wave frequencies. Enough energy is present in the wave frequencies that the turbulence signal has a clear periodicity equal to that of the waves. Ideally, the turbulent signal would exhibit no increase in energy through the wave frequencies.

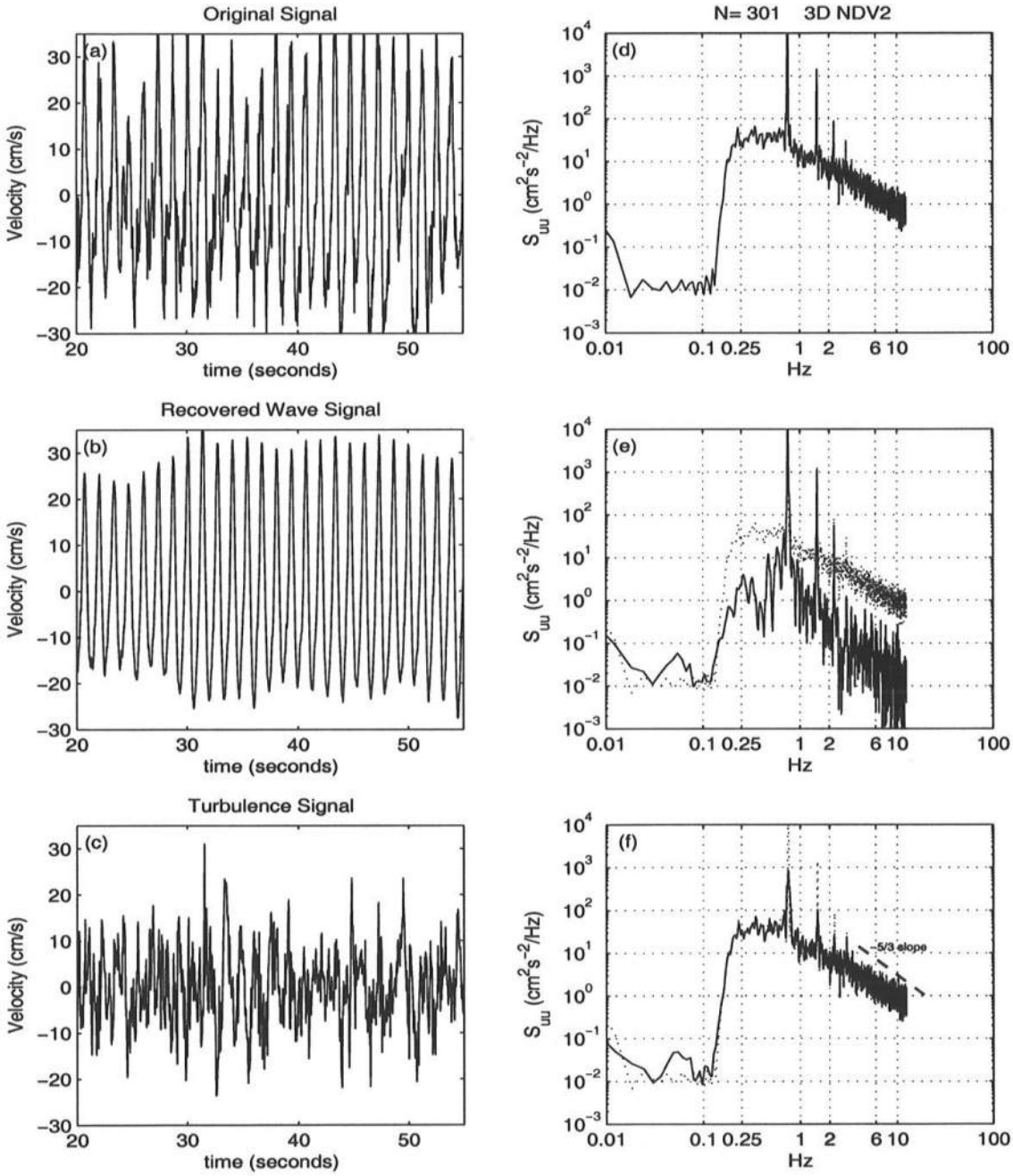

Figure 5.12: Linear filter results. Condition 3 Position D ADV 2. (a) Original signal (b) Recovered wave signal (c) Turbulence (d) Energy Spectral Density of Original Signal (e) Energy Spectral Density of Recovered Signal (f) Energy Spectral Density of Turbulence Signal

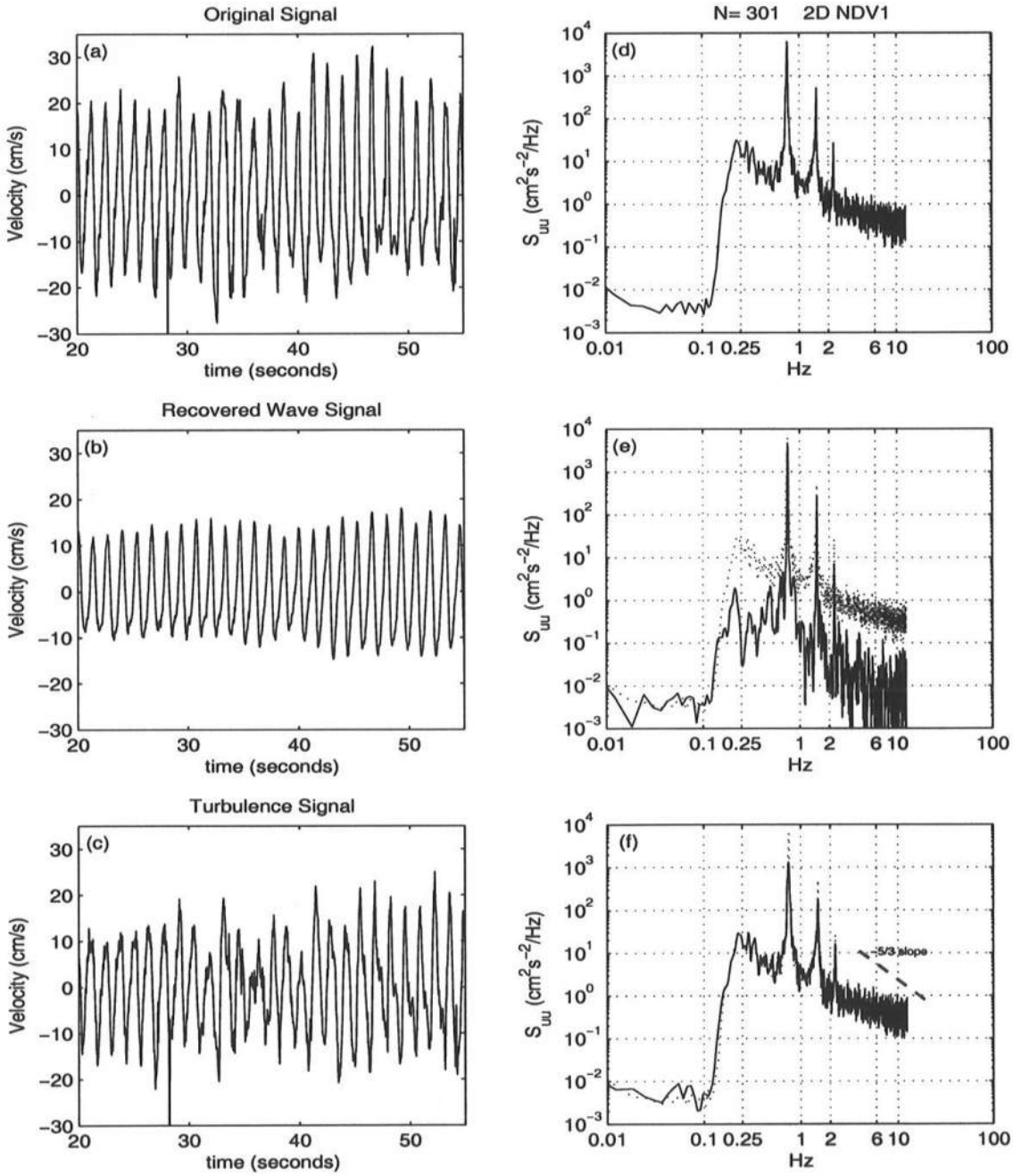

Figure 5.13: Linear filter results. Condition 2 Position D ADV 1. (a) Original signal (b) Recovered wave signal (c) Turbulence (d) Energy Spectral Density of Original Signal (e) Energy Spectral Density of Recovered Signal (f) Energy Spectral Density of Turbulence Signal

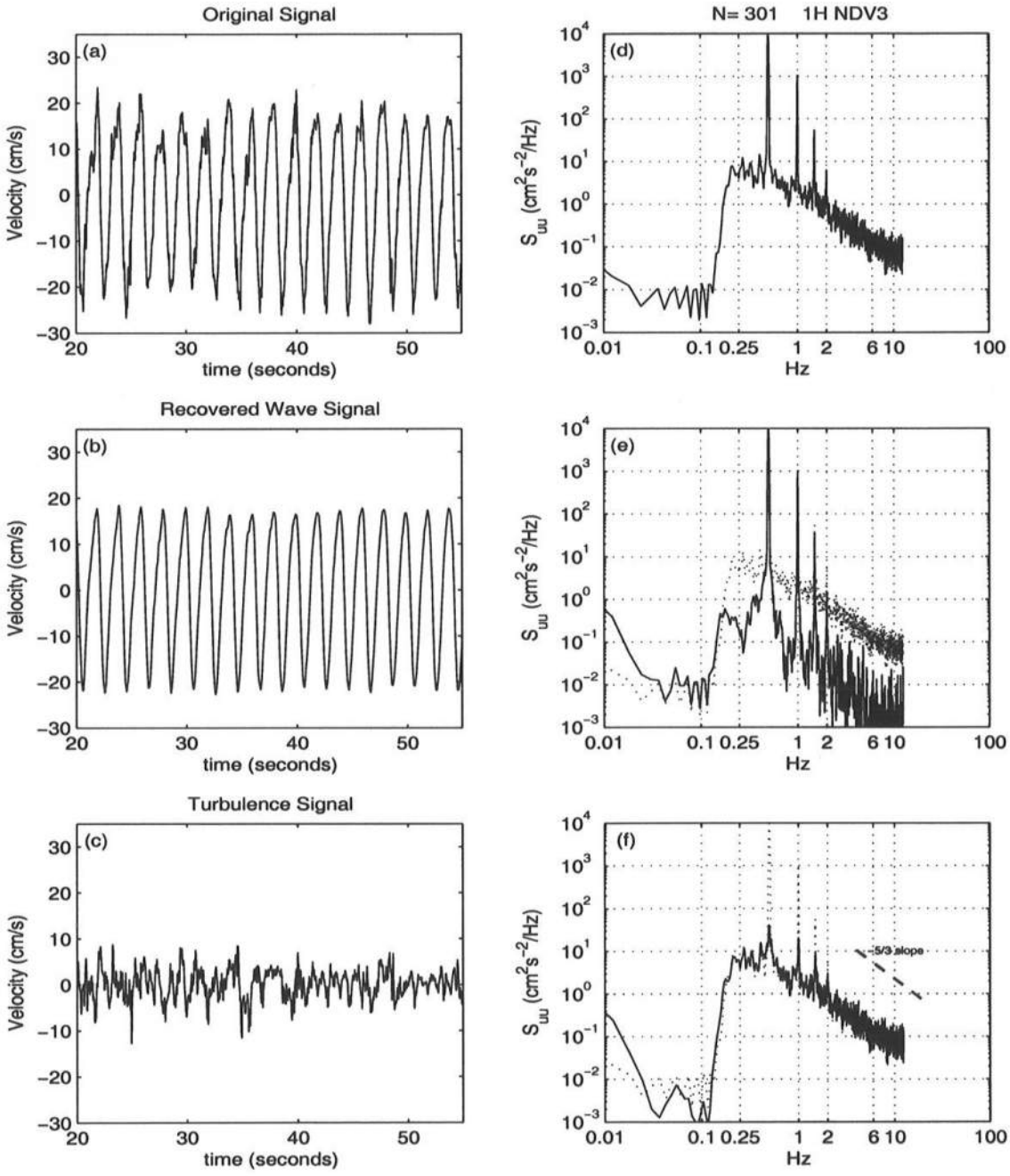

Figure 5.14: Linear filter results. Condition 1 Position H ADV 3. (a) Original signal (b) Recovered wave signal (c) Turbulence (d) Energy Spectral Density of Original Signal (e) Energy Spectral Density of Recovered Signal (f) Energy Spectral Density of Turbulence Signal

A less successful example is shown in Figure 5.13. In this case the recovered wave signal again shows a significant reduction in energy outside of the wave frequencies. The energy outside the wave frequencies is present in the turbulence signal, however there is also energy in the wave frequencies almost equal to the original signal. Indeed, the amplitude of all three signals in the time domain is the same order of magnitude. All difficulties with the linear filter were seen with data from in and around the surf zone. This is expected as the turbulence generated by wave breaking is produced periodically, as each wave passed. The periodic generation of turbulence creates a coherence between the wave motion and the turbulence. Coherence between the turbulence and wave motion violates the primary assumption of the linear filter and thus the technique fails in the surfzone.

An example showing excellent filter performance is shown in Figure 5.14. The recovered wave form is free of any high frequency oscillations and the energy spectral density shows reductions of energy outside the wave frequencies approaching 2 orders of magnitude. The turbulence signal is free of energy spikes in the wave bands and has recovered most energy outside of the wave frequencies.

Overall, the filter performs very well, where the turbulence signal has about 1 order of magnitude reduction in the primary wave peak for more than 90% of the cases tested (113 of 123 total). This method had the most difficulty with measurements made within and near the surfzone.

5.3.4 Spatial Distribution of High Frequency Turbulence

For comparison purposes, the frequency range has been segmented into three ranges (Table 5.2). The energy for frequencies $0.25Hz < f < 2Hz$ is called "mid-band", while energy in the range $2Hz < f < 6Hz$ will be referred to as "high" frequency. Summation of energy from 0.25 - 6 Hz is termed "all". These divisions will help provide a means to observe the distribution of energy, both in frequency and space.

In general, it would be expected that the high frequency energy would be sizable in the turbulence signal, while low in the recovered wave signal. Conversely, the mid-band energy should be much larger in the wave signal as compared with the turbulence.

Figure 5.15 shows the high frequency contribution from the original signal, while Figure 5.16 shows this energy is almost completely accounted for in the turbulence signal. Finally Figure 5.17 confirms that there is little high frequency energy in the recovered wave signal. The results are similar for Cases 2 and 3, with plots shown for these cases in Figures 5.18 and 5.19 respectively. It is clear from these plots that there is little high frequency energy present outside of the immediate area of the rip channel.

Table 5.2: Energy Range Definitions

Signal	Frequency Range Name	Frequencies
Original	All	0.25 - 6 Hz
Recovered Wave	Mid-range	0.25 - 2 Hz
Turbulence	High	2 - 6 Hz

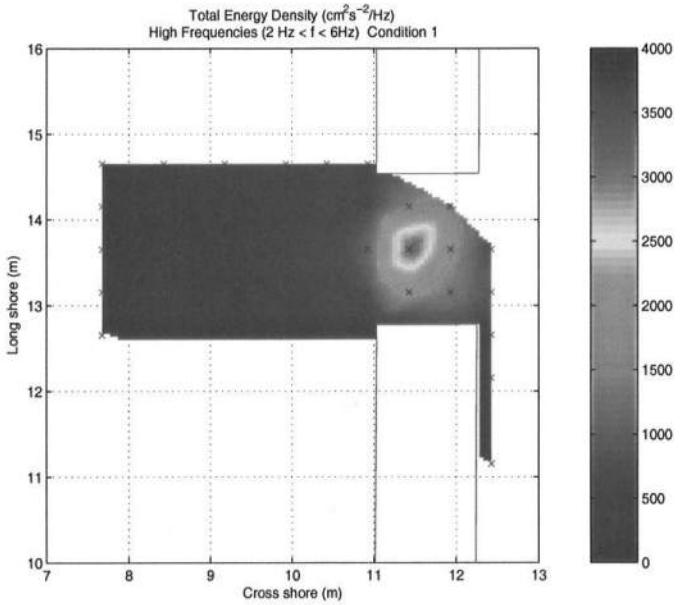

Figure 5.15: Contours of high frequency energy density from the original signal. Condition 1

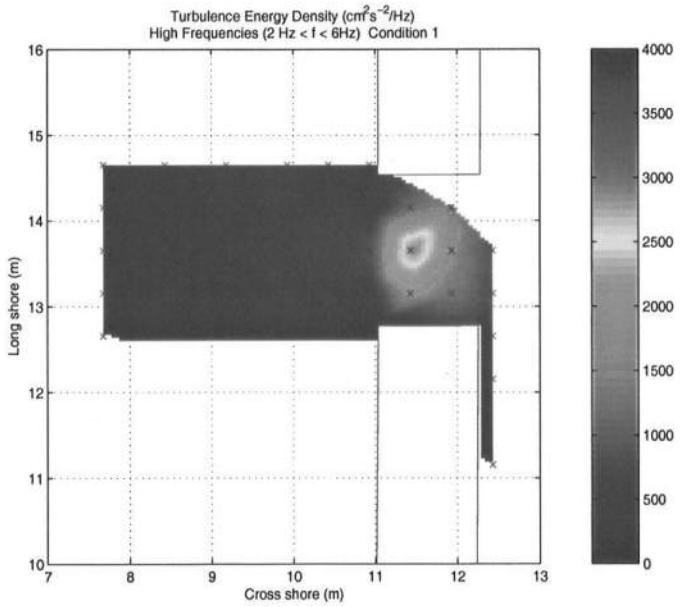

Figure 5.16: Contours of high frequency energy density from the turbulence signal. Condition 1

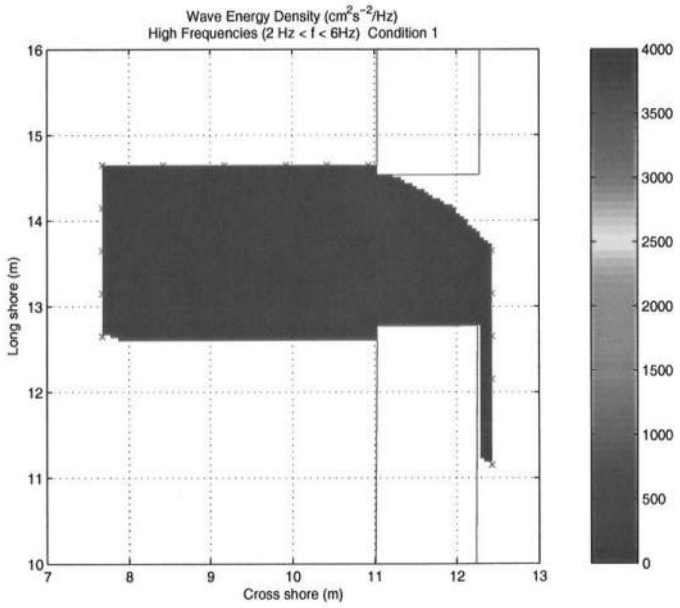

Figure 5.17: Contours of high frequency energy density from the recovered wave signal. Condition 1

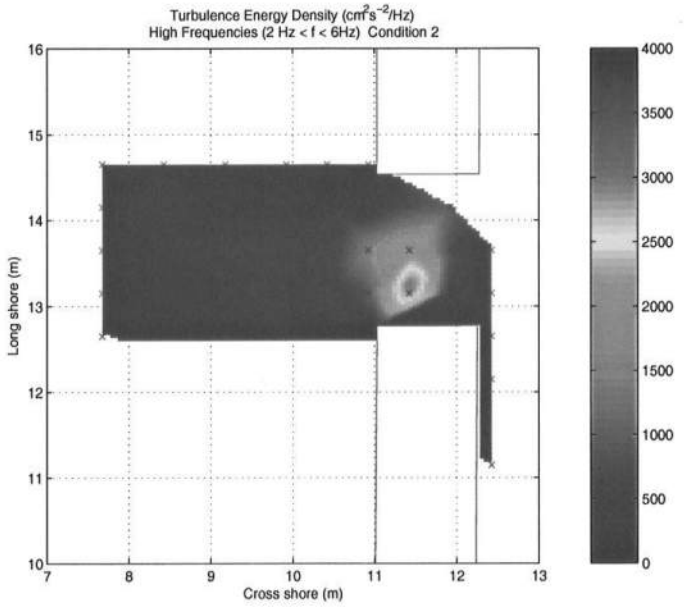

Figure 5.18: Contours of high frequency energy density from the turbulence signal. Condition 2

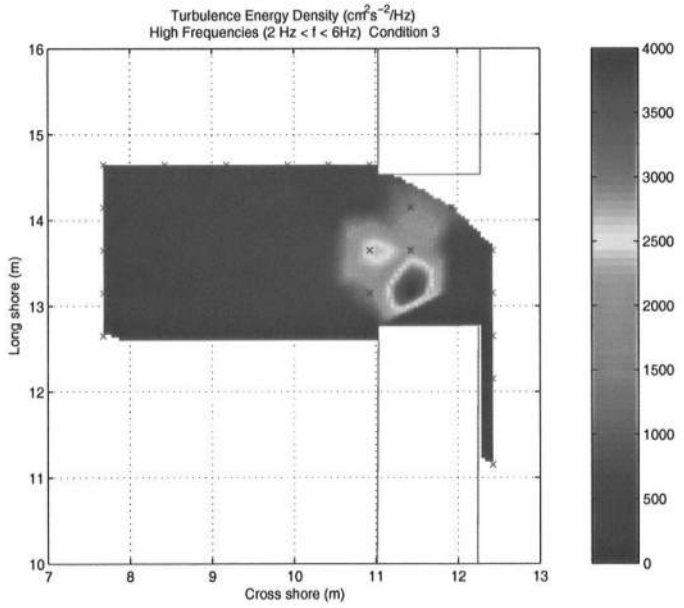

Figure 5.19: Contours of high frequency energy density from the turbulence signal. Condition 3

5.3.5 Turbulence Statistics in the Time Domain

Apart from considering turbulence in the frequency domain, one can also rely on the classic time domain definition of turbulent kinetic energy (TKE) k which is given by

$$k = \frac{1}{2}(\overline{u'^2} + \overline{v'^2} + \overline{w'^2}) \tag{5.1}$$

where u', v' and w' are the turbulent velocity fluctuations.

Beacause many experiments only record two components of the velocity, Svendsen (1987) introduced the ratio k/k' where

$$k' = \frac{1}{2}(\overline{u'^2} + \overline{w'^2}) \tag{5.2}$$

This ratio then provides an indication of the relative contribution of the transversal velocity to the total turbulence. This definition supposes, quite reasonably, that the known velocity components are the horizontal and vertical components in the plane of wave propagation. Based on the comparison of different turbulent flows, Svendsen (1987) proposed the estimate of

$$k = 1.33\ k' \tag{5.3}$$

with an error of $\pm 10\%$ such that

$$k = 1.20 - 1.46\ k' \tag{5.4}$$

.

With all three velocity components measured, it is possible to test this estimate for our flows. The values for Conditions 1-3 are shown in Figures 5.20- 5.22. Equation 5.4 is generally satisfied in the surf zone after breaking (Position A) as well as through the rip channel (Positions B and C). An exception for this region is seen for Conditions 2 and 3, where a single value over 2 is recorded. This high value is a result of an increased v' contribution to k, indicating strong transverse

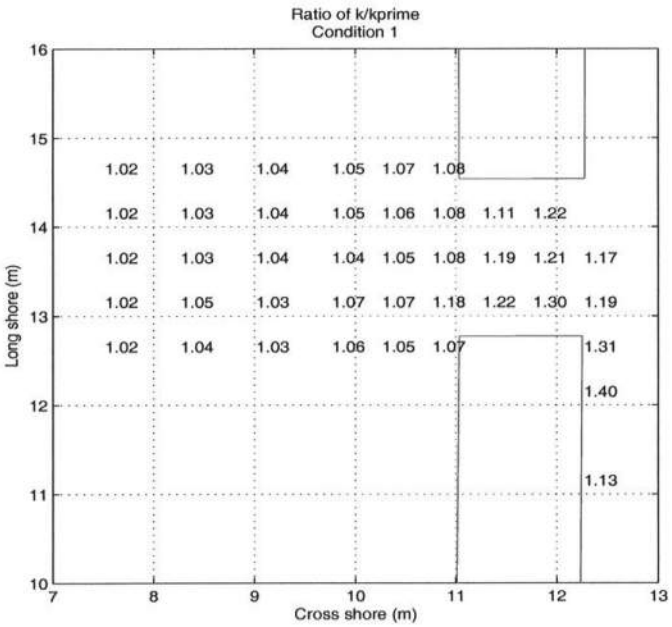

Figure 5.20: k/k' - Condition 1.

flow at this location, as the feeder current turns into the rip channel. However, immediately outside the channel the ratio value decreases and after just a meter, the ratio drops close to 1 for the entire offshore region. This would suggest that outside of the immediate area of the rip, there is essentially no turbulent velocity in the y-direction.

The contribution of each turbulent velocity component for the 3 Conditions is shown in Figures 5.23- 5.31.

We can conclude that the approximate value of k based on u' and w' as given by Svendsen (1987) is reliable for areas that exhibit high turbulence (Positions A, B and C). The results from Section 5.3.4 indicate that there is relatively little turbulence offshore of the immediate area of the rip channel. This finding is supported here as the breakdown of Svendsen's approximation occurs offshore of the rip channel, indicating non-turbulent flow. Any slower oscillations due to horizontal eddies

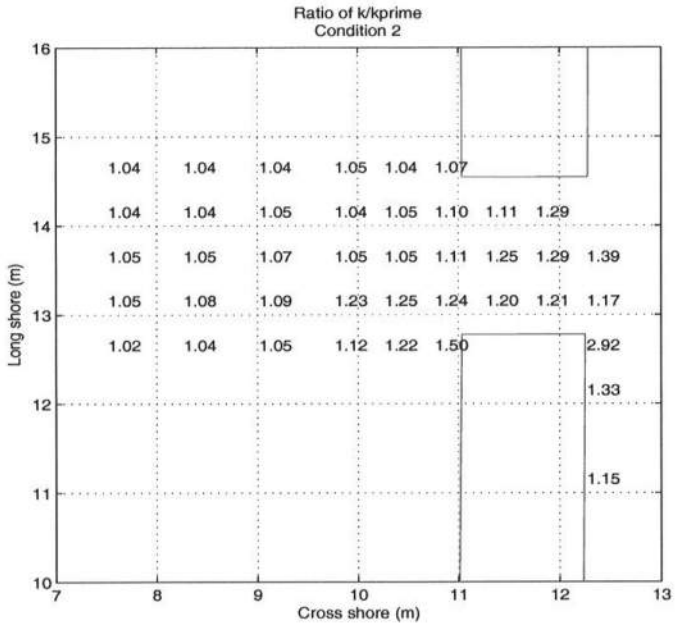

Figure 5.21: k/k' - Condition 2.

outside the rip channel would not be counted as turbulence in this work, as they are removed by the high-pass filter.

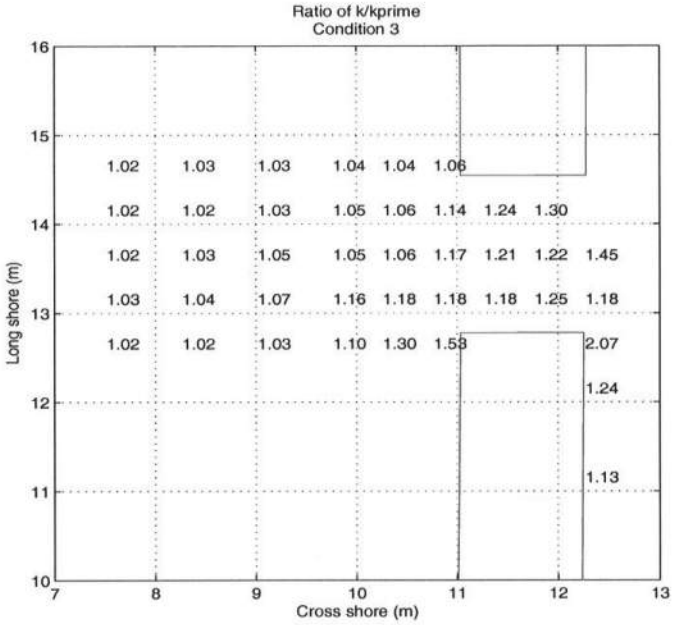

Figure 5.22: k/k' - Condition 3.

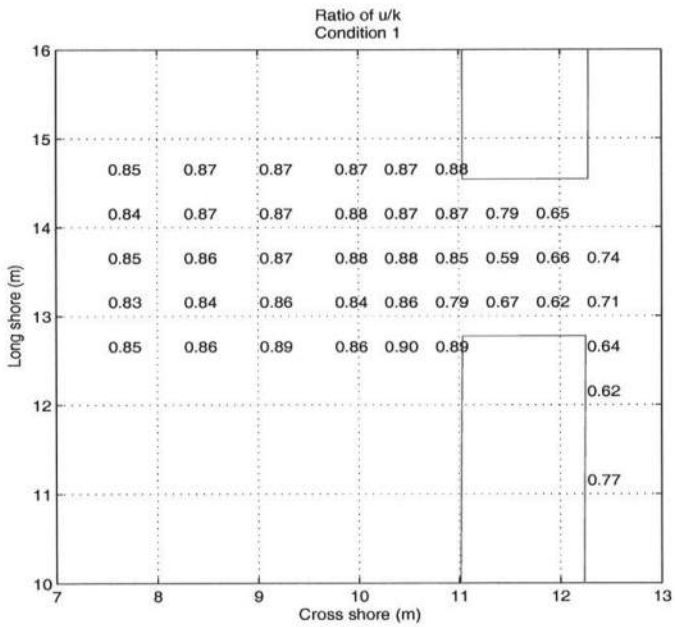

Figure 5.23: u/k - Condition 1.

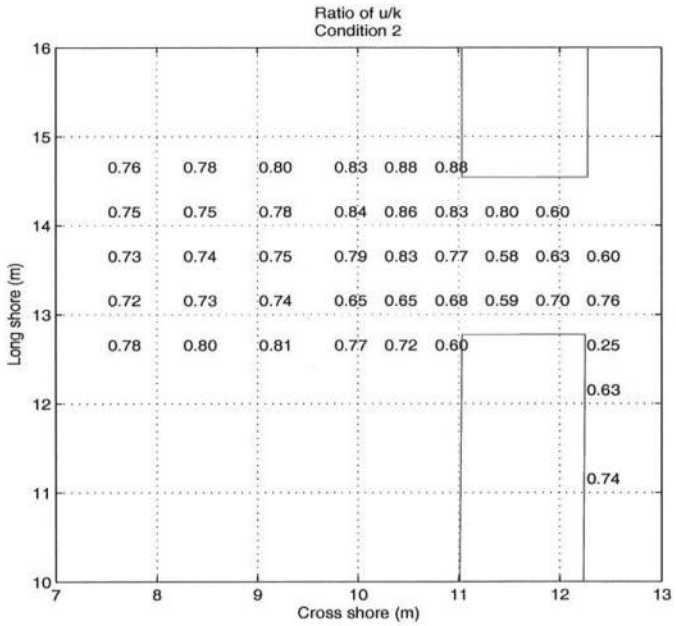

Figure 5.24: u/k - Condition 2.

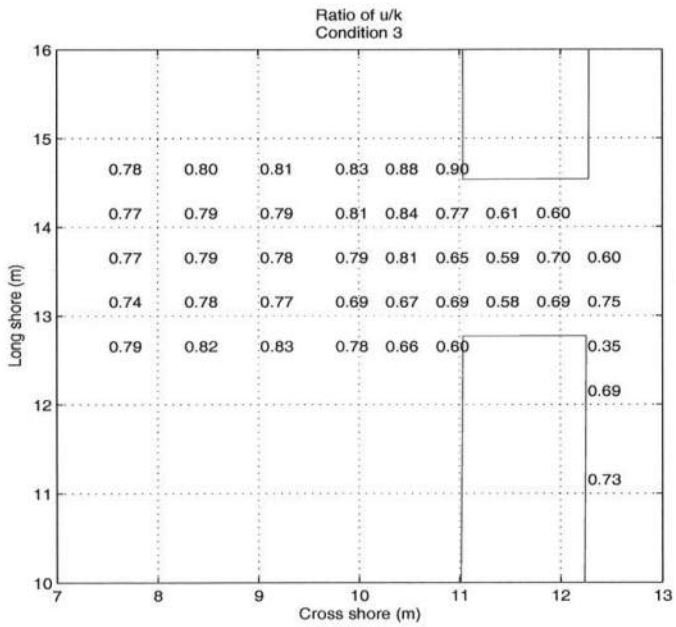

Figure 5.25: u/k - Condition 3.

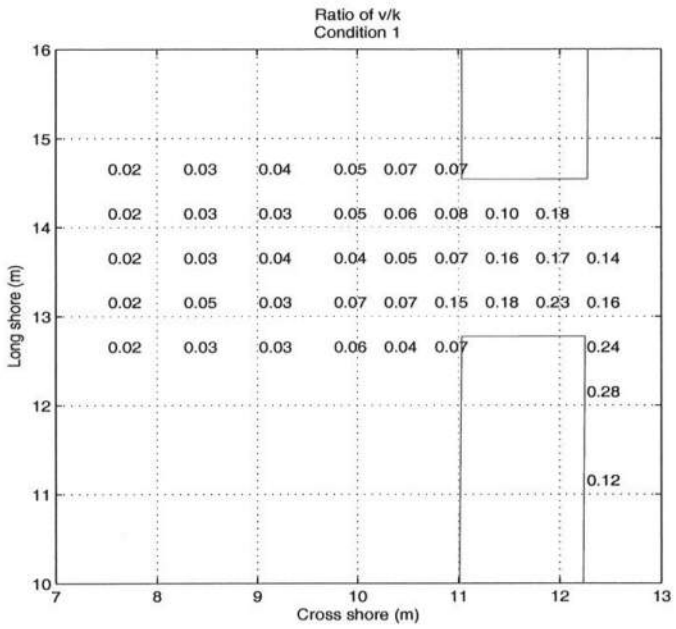

Figure 5.26: v/k - Condition 1.

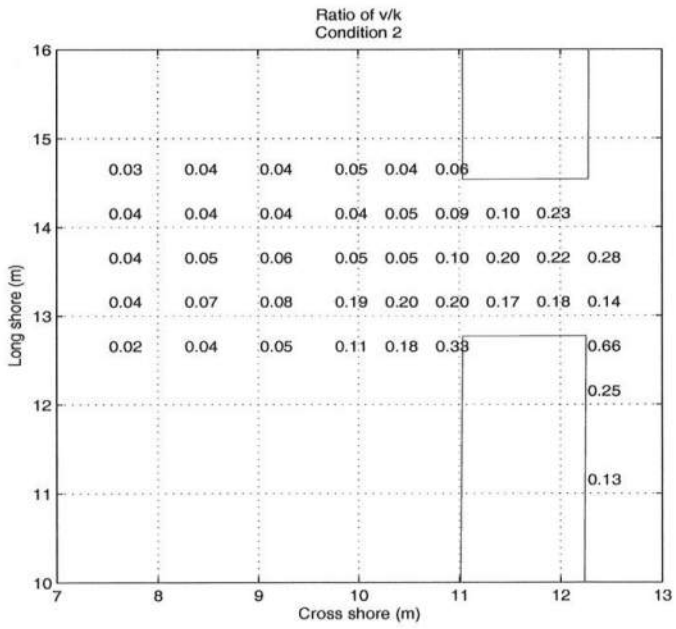

Figure 5.27: v/k - Condition 2.

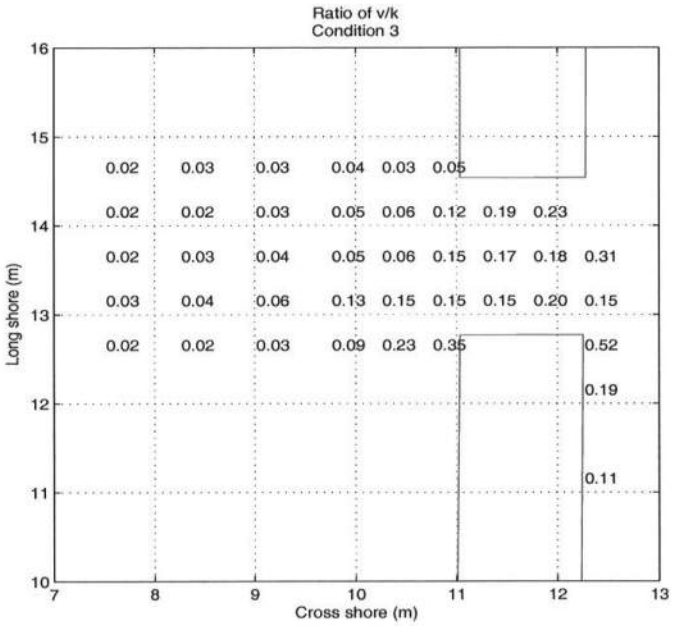

Figure 5.28: v/k - Condition 3.

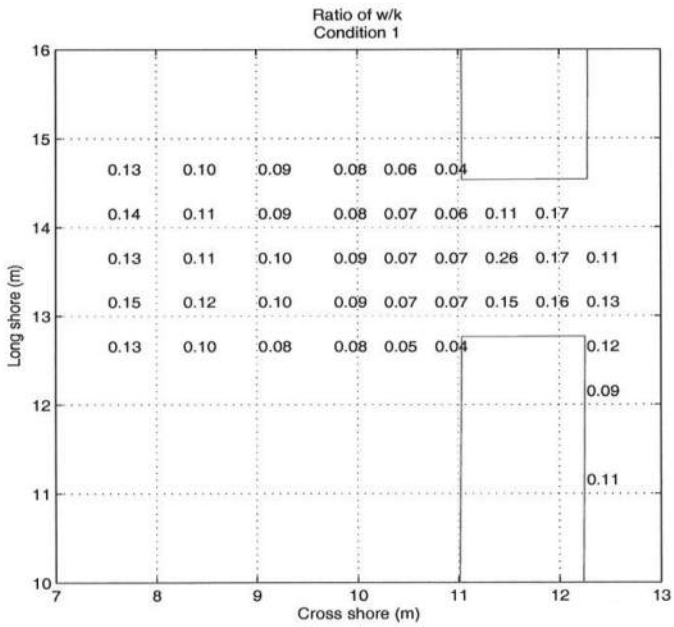

Figure 5.29: w/k - Condition 1.

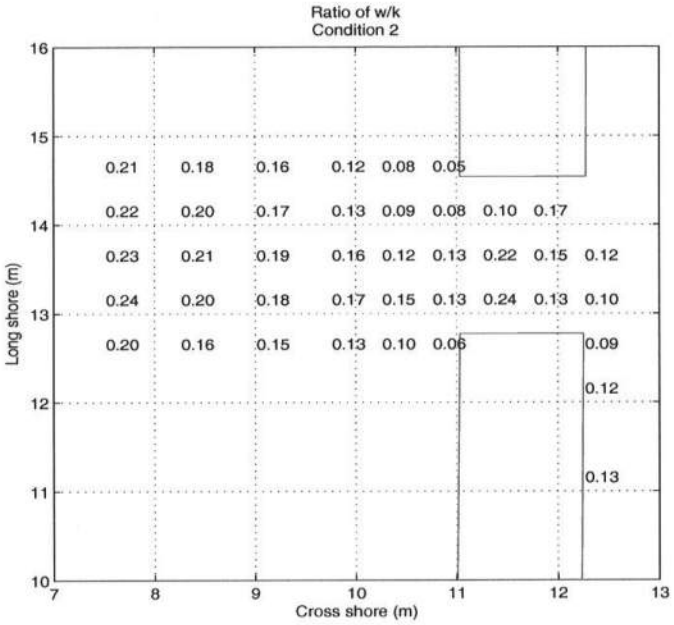

Figure 5.30: w/k - Condition 2.

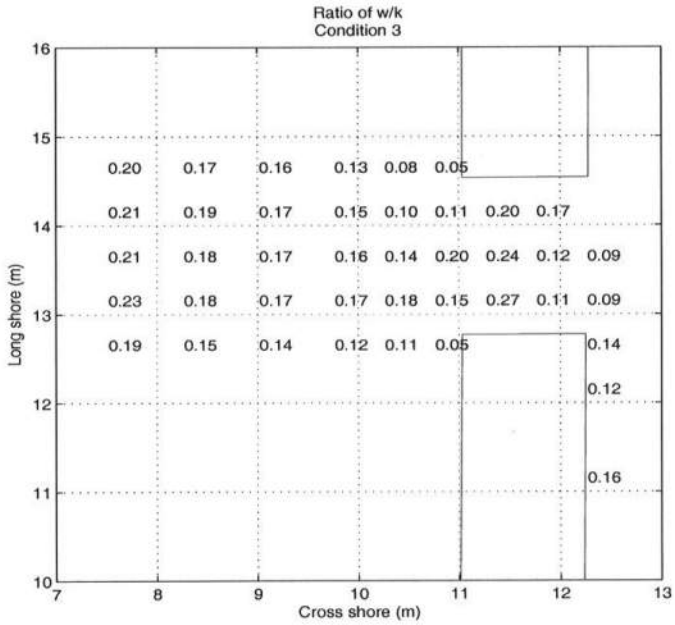

Figure 5.31: w/k - Condition 3.

5.4 Summary

The results from the wave basin experiment confirm that the linear filter technique works under a range of flow conditions. Some difficulties were encountered with data within the surf zone, which is expected as the turbulence generated by breaking is produced with each passing wave. This periodic generation of turbulence creates a coherence between the wave motion and the turbulence that it has generated through breaking. Thus the linear filter fails in the surf zone. The observations of the spatial distribution of high frequency turbulence reveal that only small amounts of high frequency ($2Hz < f < 6Hz$) energy exist outside of the the rip channel. Despite the strong offshore directed flow, virtually no high frequency energy is advected offshore of the immediate area of the rip channel. This finding is confirmed after considering frequency in the time domain. Svendsen (1987) introduced an estimate of the 3 dimensional TKE which is based on only 2 components of the velocity. This estimate was realized for those regions of the flow which exhibited high turbulence levels, namely within the surfzone and just prior to breaking. Svendsen's approximation was invalid outside of the rip channel, revealing that very low turbulence levels are present.

Chapter 6

CONCLUSIONS

The importance of understanding the flows that occur in our coastal oceans is unquestionable. Improved numerical models have allowed for improved predictions of coastal hydrodynamics and the movements of the sandy coastline. One difficulty in any hydraulic modeling is the treatment of turbulence. This work has analyzed laboratory measurements of turbulence outside of and through the surf zone and in the presence of rip currents.

The experiments reveal that despite the strong offshore flow from the rip, negligible amounts of high frequency energy are present outside the surf zone. High frequency turbulence is restricted primarily to the surf zone and just inside the rip channels. The estimate of the ratio between turbulent kinetic energy components proposed by Svendsen (1987) is found to be applicable throughout the surf zone and rip channels, where the flow is highly turbulent. This estimate only fails if there is a strong transverse component to the velocity, such as where the feeder currents turn to flow offshore in the rip.

A second focus of this work was the evaluation of the linear filter technique introduced by Shaw & Trowbridge (2001) for the separation of turbulence from a data record which also contains mean flow information and wave orbital velocities. The linear filter approach utilizes velocity records from two locations and is based on the assumption that organized wave motion in the two velocity records will be highly coherent while the random turbulent fluctuations will be incoherent.

Initial flume tests indicated that under monochromatic wave conditions, the linear filter is successful at uncoupling the turbulence signal from the organized wave motion. A gauge separation distance of 1 m was found to be close enough to leave wave induced velocities highly coherent while having the turbulent fluctuations be incoherent. It was determined that the the number of filter weights N should be chosen such that Ndt is equal to 2-6 times the wave period of interest.

The results from the wave basin experiment confirmed that the linear filter technique works under a range of flow conditions and that it provides a useful approach for extraction of the turbulence signal from the data record. Some difficulty was encountered with data taken within the surf zone. The method provided at least an order of magnitude reduction in energy within the primary wave frequencies for approximately 90% of the recorded data.

Bibliography

Blackwelder, R. & Kaplan, R. (1976). On the wall structure of the turbulent boundary layer. *Journal of Fluid Mechanics*, **76**, 80–112.

Dalrymple, R. A. (1989). Directional wavemaker theory with sidewall reflection. *Journal of Hydraulic Research*, **27**, 23–34.

Emery, W. J. & Thomson, Richard, E. (2001). *Data Analysis Methods in Physical Oceanography.* Elsevier, 2nd edition. 638 pp.

George, R., Flick, R., & Guza, R. (1994). Observations of turbulence in the surf zone. *Journal of Geophysical Research*, **99**(C1), 801–810.

Grant, W. & Madsen, O. (1986). The continental-shelf bottom boundary layer. *Annual Review of Fluid Mechanics*, **18**, 265–305.

Hattori, M. & Aono, T. (1985). Experimental study on turbulence structures under spilling breakers. In Y. Toba and H. Mitsuyasu, editors, *The Ocean Surface.* D. Reidel, Hingham, MA.

Haykin, S. (1996). *Adaptive Filter Theory.* Prentice Hall, 3rd edition. 969 pp.

Longo, S., Petti, M., & Losada, I. (2002). Turbulence in the swash and surf zones: a review. *Coastal Engineering*, **45**, 129–147.

Nadaoka, K. & Kondoh, T. (1982). Laboratory measurements of velocity field structure in the surf zone by ldv. *Coastal Engineering Japan*, **25**, 125–145.

Nadaoka, K., Hino, M., & Koyano, Y. (1989). Structure of the turbulent flow field under breaking waves in the surf zone. *Journal of Fluid Mechanics*, **204**, 359–387.

Pedersen, C., Deigaard, R., & Sutherland, J. (1998). Measurements of the vertical correlation in turbulence under broken waves. *Coastal Engineering*, **35**, 231–249.

Petti, M. & Longo, S. (2001). Turbulence experiments in the swash zone. *Coastal Engineering*, **43**, 1–24.

Rodriguez, A., Sánchez-Arcilla, A., Redondo, J., & Mosso, C. (1999). Macroturbulence measurements with electromagnetic and ultrasonic sensors: a comparison under high-turbulent flows. *Experiments in Fluids*, **27**, 31–42.

Shaw, W. & Trowbridge, J. (2001). The direct estimation of near-bottom turbulent fluxes in the presence of energetic wave motions. *Journal of Atmospheric and Oceanic Technology*, **18**, 1540–1557.

Shaw, W., Trowbridge, J., & Williams, A. (2001). The budgets of turbulent kinetic energy and scalar variance in the continental shelf bottom boundary layer. *Journal of Geophysical Research*, **106**, 9551–9564.

Stive, M. & Wind, H. (1982). A study of radiation stress and setup in the nearshore region. *Coastal Engineering*, **6**, 1–25.

Svendsen, I. (1987). Analysis of surf zone turbulence. *Journal of Geophysical Research*, **37**, 5115–5124.

Tennekes, H. & Lumley, J. (1972). *A First Course in Turbulence.* The MIT Press. 300 pp.

Thompson, R. (1979). Coherence significance levels. *Journal of Atmospheric Sciences*, **36**, 2020–2021.

Thornton, E. (1979). Energetics of breaking waves within the surf zone. *Journal of Geophysical Research*, **84**, 4931–4938.

Ting, F. (2002). Laboratory study of wave and turbulence characteristics in narrow-band irregular breaking waves. *Coastal Engineering*, **46**, 291–313.

Ting, F. & Kirby, J. (1994). Observation of undertow and turbulence in a laboratory surf zone. *Coastal Engineering*, **24**, 51–80.

Ting, F. & Kirby, J. (1995). Dynamics of surf-zone turbulence in a strong plunging breaker. *Coastal Engineering*, **24**, 177–204.

Ting, F. & Kirby, J. (1996). Dynamics of surf-zone turbulence in a spilling breaker. *Coastal Engineering*, **27**, 131–160.

Trowbridge, J., Geyer, W., Bowen, M., & Williams, A. (1999). Near-bottom turbulence measurements in a partially mixed estuary: Turbulent energy balance, velocity structure, and along-channel momentum balance. *Journal of Physical Oceanography*, **29**, 3056–3072.

Welch, P. D. (1967). The use of fast fourier transform for the estimation of power spectra: A method based on time averaging over short, modified periodograms. *IEEE Trans. Audio Electroacoust.*, (AU-15), 70–73.

Wiegel, R. L. (1964). *Oceanographical Engineering.* Prentice Hall. 532 pp.

Wilcox, D. C. (1998). *Turbulence Modeling for CFD.* DCW Industries, 2nd edition. 540 pp.

Wolf, J. (1999). The estimation of shear stresses from near-bed turbulent velocities for combined wave-current flows. *Coastal Engineering*, **37**, 529–543.